

# Surface and Subsurface Dipole Variability in the Indian Ocean and Its Relation with ENSO

Toshiaki Shinoda

NOAA-CIRES Climate Diagnostics Center

325 Broadway

Boulder, CO 80305

toshiaki.shinoda@noaa.gov

Fax: 303-497-6449

Tel: 303-497-4295

Harry H. Hendon

Bureau of Meteorology Research Centre

PO Box 1289K, Melbourne 3001, AUSTRALIA

Michael A. Alexander

NOAA-CIRES Climate Diagnostics Center

325 Broadway

Boulder, CO 80305

Deep Sea Research (accepted)

January 22, 2004

## Abstract

An ocean general circulation model, forced with observed winds for the period 1958-97, was used to examine surface and subsurface temperature variability in the Indian Ocean and its relation to ENSO. Empirical orthogonal function (EOF) analysis of temperature anomalies in the equatorial longitude-depth plane indicates that the leading mode of variability has a dipole character, with strongest loadings in the thermocline and more modest loadings at the surface. The subsurface dipole is weakly correlated with Nino3.4 SST. However, the subsurface dipole is well correlated with dipole variability at the surface, which itself is well correlated with ENSO. These results indicate that “dipole” variability that is independent of ENSO is more prominent at depth than in the SST. While the influence of ENSO on subsurface variability is detectable, the ENSO-induced surface dipole is primarily controlled by surface heat fluxes. On the other hand, subsurface variations play an important role for surface dipole events that are independent of ENSO. This is especially true in the eastern Indian Ocean where the strong surface cooling in late summer is generated by upwelling and horizontal heat advection in response to basin-wide surface easterlies.

## Keywords

Upper ocean process

Indian Ocean

# 1. Introduction

The dominant pattern of interannual variation of sea surface temperature (SST) in the tropical Indian Ocean varies with season. During boreal winter and spring anomalies tend to be same-signed throughout the basin, while during late boreal summer and autumn a zonal dipole structure predominates (e.g., Saji et al. 1999; Baquero-Bernal et al. 2002; Shinoda et al. 2004). The basin-scale mode is thought to result from the lagged response to mature ENSO conditions in the Pacific (e.g., Klein et al. 1999). Origins of the dipole structure are controversial.

The dipole structure is readily identified by empirical orthogonal function (EOF) analysis of seasonal mean SST (e.g., Shinoda et al. 2004). Figure 1a shows the leading EOF of September-October-November (SON) mean SST based on the Reynolds and Smith (1994) weekly analyses for the period 1982-1999. Similar to the leading mode computed by Shinoda et al. (2004) based on the Smith et al. (1996) reconstructed SST for the period 1950-1999, the leading EOF has strongest loadings near and to the south of the equator in the eastern portion of the basin, with oppositely signed, but weaker, loadings covering most of the western portion of the basin. While a semantical debate exists as to whether this zonally out-of-phase behavior warrants being described as a dipole (e.g., Hastenrath 2002), its occurrence is intimately tied to zonal wind anomalies in the central Indian Ocean and rainfall anomalies in eastern Africa and Indonesia (e.g., Flohn 1986; Hastenrath et al. 1993; Saji et al. 1999; Hendon 2003).

There is also an ongoing argument as to whether this dipole structure arises from coupled behavior inherent to the Indian Ocean (e.g., Saji et al. 1999; Webster et al. 1999) or whether it is driven remotely by ENSO variability in the tropical Pacific (e.g., Baquero-Bernal et al. 2002; Shinoda et al. 2004). The strong correlation (0.74)

of the leading EOF of SST in SON with the Nino3.4 SST index (Fig. 1b) provides persuasive evidence that ENSO is largely responsible for its occurrence. Note, that the strength of the correlation with ENSO varies somewhat with the analysis period and technique. For instance, Shinoda et al. (2004) show that the leading EOF of SST for SON based on the Smith et al. (1996) data for the period 1950-1999 is 0.61.

In the paradigm of the atmospheric bridge (e.g., Alexander et al. 2002; Lau and Nath 2003; Shinoda et al. 2004), ENSO affects the Indian Ocean because the upward branch of the Walker circulation shifts eastward towards the date line (e.g., Rasmusson and Carpenter 1982, Latif and Barnett 1995), resulting in anomalous easterlies and suppressed rainfall over Indonesia and the eastern Indian Ocean. These easterly anomalies during late summer and autumn enhance the mean easterly winds in the Indonesian region, resulting in anomalous evaporative cooling in the eastern Indian Ocean. The easterlies also promote coastal upwelling off of Sumatra and Java (e.g., Vinayachandran et al. 2002) and generate westward propagating Rossby waves, which suppress the thermocline and promote surface warming (together with enhanced insolation) to the west (e.g., Chambers et al. 1999; Murtugudde and Busalacchi 1999, Murtugudde et al. 2000, Xie et al. 2001). Once the Australian monsoon onsets in December and upwelling off of Sumatra and Java ceases, the same easterly anomalies then act to reduce the wind speed in the eastern Indian Ocean and, in conjunction with enhanced insolation due to reduced convective cloud cover, SSTs rapidly warm. A basin-scale warm anomaly develops by boreal spring (e.g. Klein et al. 1999, Venzke et al. 2000). The relative roles of subsurface ocean dynamics and surface heat flux forcing for driving the SST variation during the ENSO cycle is still unclear. However, surface heat flux forcing alone produces SST variations during ENSO that have realistic structure (at least in the eastern Indian Ocean) and amplitude and are phase-locked to the seasonal cycle in a qualitatively correct fashion (e.g., Hendon

2003, Shinoda et al. 2004).

On the other hand, a number of pronounced dipole events have developed in the absence of well defined ENSO variations in the Pacific (e.g., in 1961; Flohn 1986; Reverdin et al. 1986; Saji et al 1999), thus supporting the notion that ENSO may not be a necessary stimulus. Furthermore, dipole variability in subsurface temperatures, which is more prominent than at the surface, is less correlated with ENSO than is the surface dipole (e.g., Rao et al. 2002).

In an attempt to reconcile some of these conflicting results, we examine dipole variability in the Indian Ocean at the surface and subsurface from a 40-year integration of an ocean general circulation model (OGCM) forced with observed surface fluxes. We focus on differences in the surface and subsurface evolution during ENSO and during development of subsurface dipole events. The upper ocean heat budget is calculated in order to identify the dominant processes that control SST variations in each case.

## 2. Model Experiments

We employed output from a 40-year simulation of the National Center for Atmospheric Research ocean model (NCOM), which is based on the Geophysical Fluid Dynamics Laboratory (GFDL) Modular Ocean Model. The model is global with horizontal resolution of  $2.4^\circ$  in longitude. Meridional grid spacing smoothly increases from about  $0.6^\circ$  near the equator to about  $1.2^\circ$  at high latitude. Vertical mixing is based on the K-profile parameterization (KPP) of the upper ocean boundary layer (Large et al. 1994). Horizontal mixing is based on the mesoscale eddy parameterization described by Gent and McWilliams (1990). Anisotropic horizontal viscosity parameterization (Large et al. 2001) with enhanced viscosity close to boundaries and much weaker viscosity in the interior is also included. A detailed description of the model physics is found in Large et al. (1997), Gent et al. (1998) and Large et al. (2001).

The model was forced with surface fluxes of momentum, heat and freshwater for the period 1958-97 as described in Large et al. (1997). The wind stress was computed from the reanalysis fields produced at the National Center for Environmental Prediction (NCEP; Kalnay et al. 1996) using standard bulk formulae (Large and Pond 1982). The sensible and latent heat fluxes were estimated from NCEP surface winds, humidity, air temperature at 2m and model SST using standard air-sea transfer formula (Large and Pond 1982).

Net shortwave radiation at the surface based on cloud data from ISCCP (Bishop and Rossow 1991, Rossow and Schiffer 1991) was used when the data are available (1984-91). The ISCCP monthly climatology was used prior to 1984 and after 1991. Shortwave radiation is allowed to penetrate below the model surface using the two band approximation of Paulson and Simpson (1977). Monthly precipitation was obtained by combining MSU data (Spencer 1993) and estimates by Xie and Arkin (1996)

from 1979 to 1993, while monthly climatologies of the two datasets were used prior to 1979.

The model was integrated from the initial condition obtained from a preliminary climatological integration. The model was then run for two 40 years cycle, with the second cycle continuing from the end of the first cycle. The monthly output for the second 40-yr period integration was analyzed here. Further details of the model configuration are found at <http://www.cgd.ucar.edu/oce/yeager/40.html>.

In order to assess the model's simulation of interannual variability in the Indian Ocean, SST and 20°C isotherm depth (D20) variation (proxy for thermocline variation) in the tropical western Indian Ocean (50°E-70°E, 10°S-10°N) and eastern Indian Ocean (90°E-110°E, 10°S-0) were compared with observations. These boxes are the same as those used by Saji et al. (1999) for their investigation of surface dipole variability. Monthly mean SST anomalies from the model were compared to observed monthly mean anomalies based on the weekly analyses of Reynolds and Smith (1996) for the period 1982-97 (Fig. 2a). Interannual variations are faithfully reproduced in the model. In particular, the large cooling events in the eastern Indian Ocean during 1994 and 1997 and warming events in 1983 and 1996 are well depicted.

Thermocline variations (D20 anomalies) from the model were compared to analyses produced at the Joint Environmental Data Analysis (JEDA) Center (White et al. 1998; Fig. 2b). While the correspondence between model and observed is not as great as at the surface, much of the interannual variability is captured by the model (the correlation coefficient between model and observed is 0.70 for the eastern box and 0.62 for the western box). For instance, the anomalous shallowing of the thermocline during 1994 and its recovery in 1995 in the eastern Indian Ocean is well represented in the model. It should be noted that the data coverage of the subsurface temperature in the tropical Indian Ocean is not as good as SST, and thus there is significant

uncertainty of the observed D20 values. Overall, the model does a reasonable job of reproducing the observed interannual variability and we proceed to diagnose its nature and causes.



### 3. Subsurface and surface dipole

Previous studies have shown that the leading mode of interannual variability of upper ocean heat content and sea level in the near equatorial Indian Ocean has zonal dipole structure with greatest amplitude in boreal autumn (e.g., Chambers et al. 1999; Rao et al. 2002). The strongest loadings are within  $10\text{-}15^\circ$  of the equator and are displaced slightly into the Southern Hemisphere. This subsurface dipole variability is efficiently identified by EOF analysis of equatorially averaged temperature ( $5^\circ\text{N}\text{-}10^\circ\text{S}$ ) in the longitude-depth plane. The leading EOF for boreal fall (SON) explains 72.3% of the variance in the longitude-depth plane (Fig. 3a). The strongest loadings are in the vicinity of the thermocline, with more modest loadings at the surface. The largest amplitude is in the eastern part of the ocean around  $100^\circ\text{E}\text{-}105^\circ\text{E}$ . We will refer to this leading EOF as the subsurface dipole mode. The leading EOF for other seasons (not shown) has similar dipole structure but the explained variance is smaller (e.g., 53.4% in summer, 69.3% in winter, 54.5% in spring).

The principal component (PC) for the subsurface dipole mode in SON is displayed in Fig. 3b. Large positive excursions (i.e. cold in the east and warm in the west) occurred in 1961, 1994, and 1997, which are years previously identified by Saji et al. (1999) and Webster et al. (1999) as strong surface dipole years. Large negative excursions (warm in the east and cold in the west) occurred in 1971, 1984 and 1996, which were also previously identified as oppositely-signed surface dipole years. Also shown in Fig. 3b is the time series of the Nino3.4 index. While some large ENSO events are detectable in the PC time series (e.g., 1982, 1997), large subsurface dipole events also occur in the absence of ENSO (e.g., 1961) and some ENSO events are not evident in the PC time series (e.g., 1965, 1987). This is reflected in the modest simultaneous correlation of the two time series (0.37, Table 1).

Development of the subsurface dipole has previously been shown to be governed by Rossby and Kelvin waves forced by near-equatorial zonal winds (e.g., Murtugudde and Bussalacchi 1999; Rao et al. 2002). The tight coupling to the equatorial zonal wind is demonstrated by the high correlation of the zonal wind in the central Indian Ocean (averaged  $70^{\circ}\text{E}$ - $90^{\circ}\text{E}$ ,  $5^{\circ}\text{N}$ - $5^{\circ}\text{S}$ ) with the PC of the subsurface dipole mode (-0.87, Table 1; the zonal wind time series, with sign flipped, is shown as long dashed curve in Fig. 3b).

The association with Rossby and Kelvin waves is inferred from the regression of D20 anomalies onto the subsurface dipole time series (Fig. 4a). This structure is consistent with that produced by the adjustment of the thermocline to imposed zonal winds across the center of basin (e.g., McCreary and Anderson 1984). In association with enhanced equatorial easterlies (Fig. 3b), the suppressed thermocline in the western Indian Ocean takes the form of a downwelling Rossby wave, with equatorially-symmetric depth anomalies centered at about  $75^{\circ}\text{E}$ . To the east, the elevated thermocline takes the form of an upwelling Kelvin wave, which appears to travel poleward along the eastern boundary as a coastally trapped Kelvin wave and also reflects from the eastern boundary resulting in westward propagating upwelling Rossby waves. Further description of the evolution of these thermocline anomalies is provided in Sec. 4.

The expression of the subsurface dipole mode at the surface is indicated by the regression of SST onto the PC of the subsurface dipole (Fig. 4b). While subsurface structure is nearly equatorially symmetric (Fig. 4a), the associated SST anomaly is skewed to the Southern Hemisphere, especially in the eastern portion of the basin. This SST structure is similar to that described by Saji et al (1999) and Webster et al. (1999). It also bears some resemblance to the leading EOF of SST during SON (e.g., Fig. 1 and Shinoda et al. 2004), but there are some notable discrepancies.

The leading EOF of SST has largest loadings in the far eastern Indian Ocean, with more modest, oppositely-signed, anomalies in the west. The SST anomaly associated with the subsurface dipole has larger amplitude in the west, and along the equator in the east. The strong correlations between local SST and the subsurface dipole (i.e., magnitude greater than 0.8 in the far east and 0.7 in the far west; not shown) does suggest that subsurface dynamics may play a prominent role for driving SST variations.

EOFs were also computed for the model SST anomalies in the Indian Ocean (Fig. 5a). The leading EOF for SON, which captures 41.4% of the variance, also has the dipole structure that is similar to observed leading EOF of SST based on a shorter record (Fig. 1) and to that computed with a longer record (e.g., Shinoda et al. 2004). The PC of the leading EOF of model SST is well correlated with the PC calculated from the observed SST (Smith et al. 1996) for the period 1958-97 (correlation coefficient 0.89). The PC of the leading EOF along with Nino3.4 are shown in Fig. 5b. Compared to the subsurface dipole (Fig. 3b), the leading EOF of SST is more strongly correlated with Nino3.4 (correlation 0.65, Table 1). This strong correlation is consistent with other observational analyses that have indicated a significant connection between ENSO and development of a surface dipole in boreal autumn (e.g., Baquero-Banal et al. 2002, Hendon 2003, Shinoda et al. 2004). This is confirmed by similarity of the regression of model SST onto the Nino3.4 SST index for SON (Fig. 6a) with the leading EOF of SST (Fig. 5a).

Closer inspection of Fig. 5b reveals that some surface dipole events occur in the absence of ENSO conditions in the Pacific (e.g., 1961) and some ENSO events are not associated with a pronounced surface dipole (e.g., 1965). The occurrence of surface dipole variations that are independent from ENSO appears to stem from zonal wind variations in the equatorial Indian Ocean that are also independent of ENSO. This

is seen by first considering that the leading EOF of SST is well correlated with the subsurface dipole mode (correlation = 0.78, Table 1), which emphasizes the prominent role of subsurface dynamics for driving SST variations. The partial correlation of the leading EOF of SST with the subsurface dipole, where the linear relationship with Nino3.4 SST is removed, is also large (partial correlation=0.76, Table 1). This suggests that subsurface dipole variations that are independent of ENSO are responsible for the surface dipole variations that occur in the absence of ENSO. This is substantiated by the strong partial correlation of the subsurface dipole with the surface zonal wind in the equatorial Indian Ocean once the effects of Nino3.4 have been removed (partial correlation=-0.87, Table 1). This high correlation is consistent with the somewhat weaker relationship between zonal wind in the equatorial Indian Ocean and ENSO ( $r(\text{Nino3.4}, u) = -0.6$ , Table 1) and that the surface dipole and zonal wind are still related (partial correlation=-0.69, Table 1) even after the effects of Nino3.4 are removed.

One interpretation of this analysis is that surface zonal wind variations, both dependent and independent of ENSO, are the primary driver of subsurface variability in the Indian Ocean. The zonal wind anomalies are driven both remotely by ENSO (correlation -0.6, Table 1) and locally by anomalous SST gradient in the Indian Ocean (correlation 0.81, Table 1). However, it appears that the manner in which ENSO remotely forces the zonal wind over the Indian Ocean is ultimately through the induced SST anomaly in the Indian Ocean because the correlation of zonal wind with Nino3.4 disappears if the effects of the surface dipole are removed (partial correlation -0.18, Table 1; see also Feng and Meyers 2003). On the other hand, the surface dipole in the Indian Ocean (i.e. the leading EOF of SST) can develop during ENSO but independent of the subsurface dipole, as indicated by the high partial correlation of Nino3.4 and the surface dipole EOF after the effects of the subsurface dipole are removed

(partial correlation -0.61, Table 1). This is further confirmed by regression of SST onto the Nino3.4 SST index after the effects of the subsurface dipole are removed (Fig. 6b). While the magnitude of the SST variation is reduced, the overall dipole structure is still evident. This implies that the surface dipole can develop in the absence of dynamical support from the subsurface, but, when the subsurface dipole develops, it does so in conjunction with a surface dipole.

## 4. Composite evolution of upper ocean

In the previous section, we showed that subsurface temperature variability in the equatorial Indian Ocean during SON is dominated by a zonal dipole, which is more independent of ENSO than is dipole variability at the surface. However, dipole variation of SST in the absence of ENSO is evident. Furthermore, the relationship between the strength of ENSO and the strength of the SST dipole during SON is not linear: some large ENSO events are associated with modest surface dipoles while some modest ENSO events are associated with strong surface dipoles. It is possible that different mechanisms are involved in producing surface dipole variability, and these mechanisms may or may not be associated with all ENSOs. To explore these issues, we examine the subsurface and surface evolution in the Indian Ocean during ENSO and contrast that to what occurs in association with subsurface dipole variations. We do so by creating composites based on occurrence of ENSO and on occurrence of the subsurface dipole. The upper ocean heat budget is calculated in order to elucidate the important processes that control the evolution of SST in each case.

Composites are formed based on the 7 El Nino events (1965, 1969, 1972, 1976, 1982, 1987, 1991) and 5 La Nina events (1964, 1970, 1973, 1975, 1988) that were identified by Lau and Nath (2000). Note that 1997 is excluded from El Nino years since the model experiment ends in December 1997. We refer to these years as Year(0), and the following years as Year(1). The “ENSO composite” is formed as the difference between the averages over the El Nino events and the La Nina events for each variable. We also refer to this as the “warm-cold” composite.

Positive and negative subsurface dipole years are identified by excursions greater than 1 standard deviation of the time series of the subsurface dipole mode (Fig. 3b). The “subsurface dipole composite” is formed as the difference between the averages

over the positive dipole years and the negative dipole years. None of the positive dipole years (1961, 1963, 1967, 1994) include major El Nino year (1994 is regarded as a weak El Nino), and the negative dipole years (1971, 1975, 1984, 1996) only includes one La Nina event. Hence, the subsurface dipole composite depicts behavior that is mostly unrelated to ENSO.

#### 4.1. Subsurface dipole

The subsurface dipole composites for D20 and surface winds are shown in Fig. 7 for JJA and SON seasons in Year(0) and the following DJF and MAM seasons in Year(1). South-easterly surface winds across the eastern Indian Ocean are already evident in JJA. They are associated with an elevated near-equatorial thermocline in the east, which takes the form of a forced Kelvin wave, and a suppressed off-equatorial thermocline to the west, which takes the form of a forced Rossby wave. In association with strengthened equatorial south-easterlies in the east, and off-equatorial anticyclonic surface winds in the west, the downwelling Rossby wave intensifies in SON, especially south of the equator. The Kelvin wave, upon reaching the eastern boundary, appears to propagate poleward in both hemispheres as a coastally trapped Kelvin wave, and to reflect from the eastern boundary as an upwelling Rossby wave. The greatest zonal contrast across the basin occurs in SON. The south easterlies also induce upwelling along the Sumatra and Java coasts, adding to the elevation of the thermocline induced by the equatorial waves. By DJF, the southeasterly anomalies in the east have decreased, while the anticyclonic surface winds in the west continue to force the downwelling Rossby via induced Ekman convergence.

In the far east, some of the elevated thermocline along  $10^{\circ}\text{S}$  may also be associated with propagation of an ENSO-related upwelling signal into the Indian Ocean from the Pacific. Recall that the correlation of the subsurface dipole with ENSO, while weak,

is non-zero. The upwelling signal associated with the Pacific upwelling Rossby wave forced by westerly anomalies in the central Pacific appears to propagate through the Indonesian throughflow and radiates into the Indian Ocean as a Rossby wave south of Timor (e.g., Potemra 2001). It also appears to be associated with elevation of the thermocline along the western Australian coast, where it propagates southward as a coastally-trapped Kelvin wave. These subsurface signals are also seen in the ENSO composite, which is discussed below. They possibly are related to SST variations along the south-western Australian coast, but they appear not to play a prominent role for SST variations associated with the dipole.

By DJF, the forced Rossby wave in the central Indian Ocean has progressed further east. Its phase speed is much slower than expected for a free Rossby wave, consistent with the notion that it is being continually forced by induced Ekman convergence associated with anticyclonic surface winds centered near  $80^{\circ}\text{E}$ . By MAM, the southeasterlies in the east, along with the upwelling along the Java-Sumatra coasts, have weakened considerably. A downwelling Kelvin wave, which appears to emanate from reflection of the original downwelling Rossby wave at the African coast, arrives at the Sumatra coast. Rao et al. (2003) and Feng and Meyers (2003) suggest that this reflected Kelvin wave plays a prominent role in reversing the SST anomaly in the eastern portion of the basin, thus promoting an surface dipole of opposite polarity in the following year.

The SST composite for the subsurface dipole is shown in Fig. 8. In the developing stages (MAM, JJA and SON), there is a close correspondence between the subsurface anomalies and the surface anomalies: cold SSTs overlay elevated thermocline in the east and warm SSTs overlay suppressed thermocline anomalies in the west. Thus, a strong dynamical control on the SST evolution is implied. By DJF, the cold SST anomaly in the east is dramatically reduced. The warm anomaly in the west,



especially south of the equator where it overlays the Ekman ridge associated with the downwelling Rossby wave (Fig. 7), maintains its amplitude. By MAM the SST anomalies have further weakened in the east, and only the warm anomaly at  $10^{\circ}\text{S}$ ,  $70^{\circ}\text{E}$  remains in the west.

## 4.2. ENSO

The evolution of D20 and SST in the Indian Ocean associated with ENSO is shown in Figs. 9 and 10. The structure and evolution of the D20 anomalies (Fig.9) show some similarities with the subsurface dipole composite (Fig. 7), but the amplitude is weaker and the anomalies develop later. This is consistent with weaker easterly wind anomalies, especially in JJA. The equatorial easterlies and off-equatorial anticyclone south of the equator do not extend as far westward, thereby giving rise to a Rossby wave with shorter zonal wavelength. Hence, an upwelling Rossby wave is evident to the west of the main downwelling Rossby wave centered near  $80^{\circ}\text{E}$ .

The SST anomaly (Fig. 10) exhibits a dipole structure that peaks in SON (note similarity with regression pattern of SST onto Nino3.4 SST index; Fig. 6a). In contrast to the subsurface dipole composite, it gives way to a basin-scale warm anomaly by DJF (e.g., Klein et al. 1999). The spatial structure of the SST dipole anomaly during ENSO is also subtly different than that associated with the subsurface dipole. During ENSO, the SST anomaly in JJA and SON in the eastern Indian Ocean extends farther south ( $\sim 20^{\circ}\text{S}$ ), and there is almost no negative anomaly near the equator. Also, there appears to be less control of the SST by the subsurface variations. For instance negative SST anomalies show up in the east during JJA before there is evidence of an elevated thermocline there. In addition, SSTs become warm in the east in DJF, while the subsurface is still cold.

These differences are highlighted by vertical sections of the composite tempera-

ture anomalies in the eastern Indian Ocean (Fig. 11). Distinctly different variations above  $\sim 30\text{m}$  and below  $\sim 30\text{m}$  in the eastern Indian Ocean is seen in the ENSO composite, indicating little control of the SST by the subsurface. Together with having larger amplitude, the subsurface (below  $\sim 30\text{m}$ ) and surface temperature anomalies are almost in-phase for the subsurface dipole case, which suggests a strong control of the SST by the subsurface variation.

### 4.3. Upper ocean heat budget

We calculated the upper ocean heat budget in the eastern and western Indian Ocean in order to identify the dominant processes that control the interannual variations of SST during ENSO and during subsurface dipole events. The climatological mixed layer in this region is shallower than  $30\text{m}$  most of the time (e.g., Monterey and Levitus 1997), thus the heat budget of upper  $30\text{m}$  was analyzed.

The components of the surface layer heat budget (surface heat flux, vertical and horizontal heat advection and temperature tendency) in the eastern and western Indian Ocean are shown in Fig. 12 for the subsurface dipole and ENSO composites. The temperature tendency is calculated from the composite temperature. Note that the anomaly of shortwave radiation, a prominent component of the surface heat flux especially during the decay phase of the surface dipole (e.g., Hendon 2003), is negligible since climatological values are prescribed for most of the period (Sec. 2). Thus, the surface heat flux variation is primarily caused by the latent heat flux.

In the eastern Indian Ocean, surface heat fluxes are the dominant term in the heat budget for the typical ENSO event, corroborating previous studies that have indicated that dipole variations are primarily controlled by surface heat fluxes (e.g., Hendon 2003, Shinoda et al. 2004). Increased latent heat flux (evaporative cooling) from July to September acts to cool the surface while decreased latent heat flux

from November to February acts to warm the surface. The warming beginning in November is also promoted by positive horizontal advection, which is generated by the mean positive zonal gradient of SST and an anomalous westward current driven by anomalous easterlies during October-January. Vertical advection (upwelling) is most negative in October and November, at which time it opposes the horizontal advection and, in fact, is out of phase with the mixed layer temperature tendency. Prior to this, vertical advection is weak and appears not to be important for development of the cold anomaly in late summer-early autumn.

For the subsurface dipole composite, initial cooling in the east during June and July is caused by weak negative surface heat flux anomaly and upwelling. However, the surface heat flux then becomes positive in August and acts to damp the negative temperature tendency. The peak cooling in August and September results from upwelling and horizontal advection. As for the ENSO composite, the subsequent warming from October onwards is largely driven by positive surface heat flux and positive horizontal temperature advection, while upwelling continues to act to cool.

Interpretation of the heat budget in the western Indian Ocean is not as simple as in the east. In general, all processes are important. The surface heat flux contributes most to the warming during fall for the ENSO composite. For the subsurface dipole composite, horizontal advection of heat is significant during September-October, vertical advection becomes large during November, and the surface heat flux becomes negative in December and January.

The above analysis suggests that the surface heat flux and advective processes work together during a typical ENSO event to produce the initial SST anomaly in the eastern Indian Ocean during summer and autumn. On the other hand, much stronger advective processes overcome an oppositely signed surface heat flux tendency to drive the SST anomaly during a typical subsurface dipole event. This contrasting

behavior is summarized in Fig. 13 and 14, which show the regressions in July-August-September (coincident with the peak negative SST tendency in the east) of surface heat flux and advective tendency (summation of vertical and horizontal advective tendencies) onto the Nino3.4 SST index and PC1 of the subsurface dipole, respectively. The advective tendency, while stronger and more coherent for the subsurface dipole case, has similar structure in each case, with strongest cooling in the east and along the Java and Sumatra coasts. However, the differing behavior of the heat flux in the eastern Indian Ocean is dramatic, with widespread cooling across the south east for ENSO and warming for the subsurface dipole.

This marked contrast results from the differing latent heat flux anomalies. In both cases, the surface wind anomaly is easterly, which increases the windspeed south of the equator at this time of year. For the ENSO case, this increases the latent heat flux. Despite the increased windspeed, the latent heat flux decreases for the dipole case because of the sharp decrease in SST, which lowers the saturated specific humidity at the surface.

Development of a weak warm SST anomaly north of the equator in the east in summer and autumn, despite significant negative D20 anomalies (e.g., Figs. 7 and 9), is also explained by Fig. 13 and 14. The surface heat flux anomaly is mostly positive and the advective tendency is either weak or positive. The positive surface heat flux results because the easterly anomalies (e.g. Figs. 7 and 9) tend to oppose the mean winds north of the equator at this time of year. Hence, the windspeed and latent heat flux are reduced. Thus, the cold surface anomaly associated with the surface dipole tends to be confined south of the equator and along the Java and Sumatra coasts.

The above analyses suggest that there are two varieties of SST dipole: one is governed by the surface heat flux variations remotely forced by ENSO and the other is governed by ocean dynamics driven by winds associated with the induced SST

anomaly in the Indian Ocean. In both cases, peak development of the surface dipole in SON is accompanied by easterly anomalies in the equatorial Indian Ocean, which force Rossby and Kelvin waves. D20 and SST anomalies are relatively large and co-evolve during subsurface dipole events, while the D20 and SST anomalies are smaller and tend to evolve independent during most ENSO events. Stronger easterly anomalies, which begin earlier in the summer, drive larger D20 anomalies during subsurface dipole events. On the other hand, the latent heat flux anomaly in the eastern Indian Ocean is determined both by local winds and SSTs. The wind speed anomaly in the eastern Indian Ocean associated with ENSO has the same sign as during a subsurface dipole event, but is typically about half as strong. The eastern Indian Ocean SST anomaly is also weaker. Hence, easterly anomalies promote similar subsurface anomalies in the two cases but the latent heat flux has opposite sign.

Since large thermocline anomalies develop during non-ENSO years (e.g., 1961, 1967, 1994) and the thermocline anomaly is relatively small during ENSO years (Fig. 12), the subsurface dipole is not well correlated with ENSO (Table 1). On the other hand, the SST dipole is developed in both ENSO-independent subsurface dipole years and most of the ENSO years, and thus the SST dipole is better correlated with both ENSO and the subsurface dipole (Table 1).

## 5. Conclusions

Surface and subsurface temperature variability in the equatorial Indian Ocean and its relation to ENSO was examined using output from an OGCM forced with observed surface fluxes. Emphasis was given to dipole variations, which are prominent in SON at the surface but occur year round in the subsurface. The surface dipole is strongly correlated with ENSO, while the subsurface dipole is mostly independent of ENSO.

Composites based on occurrences of ENSO and the subsurface dipole were formed to highlight the differing evolutions. The composite upper ocean heat budget indicates that ENSO typically induces a relatively shallow surface dipole that is primarily controlled by surface heat flux variations. Wind-forced ocean dynamics play a dominant role for development of the SST dipole that accompanies the subsurface dipole. In particular, cooling during summer in the eastern Indian Ocean is generated by strong upwelling and horizontal heat advection, which is opposed by decreased latent heat flux. In contrast, cooling is driven by increased latent heat flux during ENSO, with less role for subsurface dynamics. In both cases, surface warming in the eastern Indian Ocean that commences in October stems from decreased upward latent heat flux and positive horizontal temperature advection, with vertical advection (upwelling) acting to oppose the warming.

Many subsurface dipole events occur independent of ENSO but some ENSO events are associated with large subsurface dipoles. This suggests that the ENSO-induced surface zonal wind anomalies in the Indian Ocean can sometimes trigger a dynamically-controlled dipole. However, surface zonal winds over the Indian Ocean are to some extent independent of ENSO. Partial correlation analysis suggests that these ENSO-independent variations of winds are coupled to the SST variations that they generate in the Indian Ocean, but it is difficult to ascertain whether the SST

variation is just a response to the winds. For instance, basin-scale surface zonal wind variations, which could drive the SST anomalies, can be generated by variations in the Australian and Indian summer monsoons and by the MJO (Madden and Julian 1972). Further study is required to understand their role in generating dipole variability in the Indian Ocean.

## Acknowledgment

We would like to acknowledge the NCAR Oceanography section for making the ocean model output available to us. We also thank two anonymous reviewers for their constructive comments. Support for this work was provided by CLIVAR-Pacific Grants from NOAA's office of Global Programs.



## References

- Alexander, M. A., I. Blade, M. Newman, J. Lanzante, N.-C. Lau, and J. Scott, 2002: The atmospheric bridge: the influence of ENSO teleconnections on air-sea interaction over the global oceans. *J. Climate*, 15, 2205-2231.
- Baquero-Bernal, A., M. Latif, and S. Legutke, 2002: On dipolelike variability of sea surface temperature in the tropical Indian Ocean. *J. Clim.*, 15, 1358-1368.
- Behera, S. K, P. S. Salvekar, and T. Yamagata, 2000: Simulation of interannual SST variability in the tropical Indian Ocean. *J. Clim.*, 13, 3487-3499.
- Bishop, J. K. B., and W. B. Rossow, 1991: Spatial and temporal variability of global surface solar irradiance. *J. Geophys. Res.*, 96, 16839-16858.
- Chambers, D. P., B. D. Tapley, and R. H. Stewart, 1999: Anomalous warming in the Indian Ocean coincident with El Nino. *J. Geophys. Res.*, 104, 3035-3047.
- Feng, M. and G. Meyers, 2003: Interannual variability in the tropical Indian Ocean: A two-year time scale of Indian Ocean Dipole, *Deep-Sea Res. II*, 50, 2263-2284.
- Flohn, H., 1986: Indonesian droughts and their teleconnections. *Berliner Geographische Studien*, 20, 251-265.
- Gent, P. R., and J. C. McWilliams, 1990: Isopycnal mixing in ocean circulation models. *J. Phys. Oceanogr.*, 20, 150-155.
- Gent, P. R., F. O. Bryan, G. Danabasoglu, S. C. Doney, W. G. Holland, W. G. Large, and J. C. McWilliams, 1998: The NCAR Climate System Model global ocean component. *J. Phys. Oceanogr.*, 11, 1287-1306.

- Hastenrath, S., A. Nicklis and L. Greischar, 1993: Atmospheric-hydrospheric mechanisms of climate anomalies in the western equatorial Indian Ocean. *J. Geophys. Res.*, 98, 20219-20235.
- Hastenrath, S., 2002: Dipoles, temperature gradients, and tropical climate anomalies. *Bull. Amer. Meteor. Soc.*, 83, 735-738.
- Hendon H. H., 2003: Indonesian rainfall variability: Impact of ENSO and local air-sea interaction. *J. Climate*, 16, 1775-1790.
- Kalnay, E., and Co-authors, 1996: The NCEP/NCAR 40-Year Reanalysis Project. *Bull. Amer. Meteor. Soc.*, 77, 437-471.
- Klein, S. A., B. J. Soden and N. C. Lau 1999: Remote sea surface temperature variations during ENSO: Evidence for a tropical atmospheric bridge. *J. Climate.*, 12, 917-932.
- Large, W. G., J. C. McWilliams and S. C. Doney, 1994: Oceanic vertical mixing: Review and a model with a nonlocal boundary layer parameterization. *Rev. Geophys.*, 32, 363-403.
- Large, W. G., G. Danabasoghu, and S. C. Doney, 1997: Sensitivity to surface forcing and boundary layer mixing in a global ocean model: annual-mean climatology. *J. Phys. Oceanogr.*, 27, 2418-2447.
- Large, W. G., J. C. McWilliam, P. R. Gent, and F. O. Bryansand, 2001: Equatorial circulation of a global ocean climate model with an isotropic horizontal viscosity. *J. Phys. Oceanogr.*, 31, 518-536.
- Large, W. G., and S. Pond, 1982: Sensible and latent heat flux measurements over the ocean. *J. Phys. Oceanogr.*, 12, 464-482

- Latif, M., and T. P. Barnett, 1995: Interactions of the Tropical Oceans. *J. Climate*, 8, 952-964.
- Lau, N. C. and M. J. Nath 2000: Impact of ENSO on the variability of the Asian-Australian monsoons as simulated in GCM experiments. *J. Climate*, 13, 4287-4309.
- Lau, N. C. and M. J. Nath 2003: Atmosphere-ocean variations in the Indo-Pacific sector during ENSO episode. *J. Climate*, 16, 3-20.
- Madden, R. A., and P. R. Julian, 1972: Description of global-scale circulation cells in the tropics with a 40-50 day period. *J. Atmos. Sci.*, 29, 1109-1123.
- McCreary, J. P., and D. T. Anderson, 1984: Simple models of El Nino and the Southern Oscillation. *Mon. Wea. Rev.*, 112, 934-946.
- Monterey, G. I., and S. Levitus, 1997: Climatological cycle of mixed layer depth in the world ocean. U.S. Gov. Printing Office, NOAA Nesdis, 5pp.
- Murtugudde, R., and A. J. Bussalacchi, 1999: Interannual variability of the dynamics and thermodynamics of the tropical Indian Ocean. *J. Climate*, 12, 2300-2326.
- Murtugudde, R., J. P. McCreary Jr. and A. J. Bussalacchi, 2000: Oceanic processes associated with anomalous events in the Indian Ocean with relevance to 1997-1998. *J. Geophys. Res.*, 105, 3295-3306.
- Paulson, C. A., and J. J. Simpson, 1977: Irradiance measurements in the upper ocean, *J. Phys. Oceanogr.*, 7, 952-956.
- Potemra, J.T., 2001: The potential role of equatorial Pacific winds on southern tropical Indian Ocean Rossby waves. *J. Geophys. Res.*, 106, 2407-2422.

- Rasmusson, E. M., and T. H. Carpenter, 1982: Variations in tropical sea surface temperature and surface wind fields associated with the Southern Oscillation/El Nino. *Mon. Wea. Rev.*, 110, 354-384.
- Rao, S. A., S. K. Behera, Y. Masumoto, and T. Yamagata, 2002: Interannual sub-surface variability in the tropical Indian Ocean with a special emphasis on the Indian Ocean dipole. *Deep Sea Res. II*, 49, 1549-1572
- Reverdin, G., D. Cadet and D. Gutzler, 1986: Interannual displacements of convection and surface circulation over the equatorial Indian Ocean. *Q. J. R. Met. Soc.*, 112, 43-67.
- Reynolds, R. W. and T. M. Smith, 1994: Improved global sea surface temperature analyses using optimum interpolation. *J. Climate*, 7, 929-948.
- Rossow, W.B., and R. A. Schiffer, 1991: ISCCP cloud data products. *Bull. Amer. Meteor. Soc.*, 72, 2-20.
- Saji, N. H., B. N. Goswami, P. N. Vinayachandran and T. Yamagata 1999: A dipole mode in the tropical Indian Ocean. *Nature*, 401, 360-363.
- Shinoda, T., M. A. Alexander, and H. H. Hendon 2004: Remote response of the Indian Ocean to interannual SST variations in the tropical Pacific. *J. Climate*, 17, 362-372.
- Smith, T. M., R. W. Reynolds, R. E. Livezey, and D. C. Strokes, 1996: Reconstruction of historical sea surface temperatures using empirical orthogonal functions. *J. Climate.*, 9, 1403-1420.
- Spencer, R.W., 1993: Global oceanic precipitation from the MSU during 1979-91 and comparisons to other climatologies. *J. Clim.*, 6, 1301-1326.

- Vinayachandran, P. N., S. Iizuka, and T. Yamagata, 2002: Indian Ocean dipole mode events in an ocean general circulation model. *Deep Sea Res. II*, 49.
- Venzke, S., M. Latif and A. Villwock 2000: The coupled ECHO-2. Part II: Indian ocean response to ENSO. *J. Clim.*, 13, 1371-1383.
- Webster, P. J., A. M. Moore J. P. Loschnig and R. R. Leben 1999: Coupled ocean-atmosphere dynamics in the Indian Ocean during 1997-98. *Nature*, 401, 356-360.
- White, W. B., S. E. Pazan, G. W. Withee, and C. Noe, 1998: Joint Environmental Data Analysis (JEDA) center for scientific quality control of upper ocean thermal data in support of TOGA and WOCE. *EOS transactions, American Geophysical Union*, 69m122-123
- Xie, P., and P. A. Arkin, 1996: Analysis of global monthly precipitation using gauge observations, satellite estimates and numerical model predictions. *J. Clim.*, 9, 531-544.
- Xie, S. P., H. Annamalai, F. A. Schott and J. P. McCreary 2001: Structure and mechanism of south Indian Ocean climate variability. *J. Clim.*, 15, 864-878.

Table 1: Correlation coefficients between PC(subsurface), PC(SST), zonal winds, and Nino3.4 SST during SON. The values with parentheses indicates partial correlations where linear relationship with the variable in parentheses is removed (see text for details)

	PC-1(subsurface)	PC-1(SST)	Zonal winds	Nino34
PC(subsurface)	1.0	0.76(Nino34)	-0.87(Nino34)	
PC(SST)	0.78	1.0	-0.69(Nino34)	0.62(subsurface)
Zonal winds	-0.87	-0.81	1.0	-0.18(SST) -0.61(subsurface)
Nino34	0.37	0.65	-0.60	1.0

## Figure captions

Figure 1: (a) The first eigenvector of the SST analysis (Reynolds and Smith 1994). (b) PC-1 (solid line) and Nino3.4 SST anomaly (dotted line). Time series are normalized by their standard deviations.

Figure 2: (a) Time series of SST anomaly from observations (dashed line) and the model (solid line) in the western Indian Ocean ( $50^{\circ}\text{E}$ - $70^{\circ}\text{E}$ ,  $10^{\circ}\text{S}$ - $10^{\circ}\text{N}$ ) (upper panel) and the eastern Indian Ocean ( $90^{\circ}\text{E}$ - $110^{\circ}\text{E}$ ,  $10^{\circ}\text{S}$ - $0$ ) (lower panel) (b) Same as (a) except for the  $20^{\circ}\text{C}$  isotherm depth anomaly.

Figure 3: (a) The first eigenvector of the temperature of longitude-depth plane for September-November. (b) PC-1 (solid line), Nino3.4 SST anomaly (dotted line) and zonal winds in the central Indian Ocean ( $70^{\circ}\text{E}$ - $90^{\circ}\text{E}$ ,  $5^{\circ}\text{N}$ - $5^{\circ}\text{S}$ ) for September-November. The positive zonal wind anomaly indicates easterly.

Figure 4: D20 (upper panel) and model SST (lower panel) regressed onto PC-1 from the EOF analysis of temperature in the equatorial longitude-depth plane. Contour intervals are 2.5 m for the D20 and  $0.1^{\circ}\text{C}$  for the SST. Areas where the explained variance is significant (95%) are shaded.

Figure 5: (a) The first eigenvector of the model SST. (b) PC-1 of the EOF analysis of model SST (solid line) and Nino3.4 SST anomaly (dotted line). Time series are normalized by their standard deviations.

Figure 6: (a) Model SST for September-November regressed onto Nino3.4 SST anomaly

(SON). The contour interval is  $0.05^{\circ}\text{C}$ . Areas where the explained variance is significant (95%) are shaded. (b) Same as (a) except the effects of the subsurface dipole are removed.

Figure 7: The subsurface dipole composite (see text for the detail) of  $20^{\circ}\text{C}$  isotherm depth and surface winds during June-August (a), September-November (b), December-February (c), and March-May (d).

Figure 8: The subsurface dipole composite of SST during June-August (a), September-November (b), December-February (c), and March-May (d).

Figure 9: The ENSO composite (see text for the detail) of  $20^{\circ}\text{C}$  isotherm depth and surface winds during June-August (a), September-November (b), December-February (c), and March-May (d).

Figure 10: The ENSO composite of SST during June-August (a), September-November (b), December-February (c), and March-May (d).

Figure 11: The ENSO composite (upper panel) and dipole composite (lower panel) of the average temperature in the eastern Indian Ocean ( $90^{\circ}\text{E}$ - $110^{\circ}\text{E}$ ,  $10^{\circ}\text{S}$ - $0$ ).

Figure 12: (a) Upper panel: The ENSO composite of temperature tendency (open circle), vertical advection of heat (closed circle), horizontal advection of heat (triangle) in the upper 30 m and net surface heat flux (closed square) in the eastern Indian Ocean. Lower panel: Same as the upper panel except for the subsurface dipole composite. (b) Same as (a) except for the western Indian Ocean.



Figure 13: (a) Surface heat flux for July-September regressed onto Nino3.4 SST anomaly (SON). The contour interval is  $1 \text{ W/m}^2$ . Areas where the explained variance is significant (95%) are shaded. The negative values indicate cooling when Nino3.4 SST anomaly is positive. (b) Same as (a) except for horizontal and vertical heat advection.

Figure 14: (a) Surface heat flux for July-September regressed onto PC-1 from the EOF analysis of temperature in the equatorial longitude-depth plane. The contour interval is  $2 \text{ W/m}^2$ . Areas where the explained variance is significant (95%) are shaded. The negative values indicate cooling when PC-1 is positive. (b) Same as (a) except for horizontal and vertical heat advection.



Fig. 1

(a)

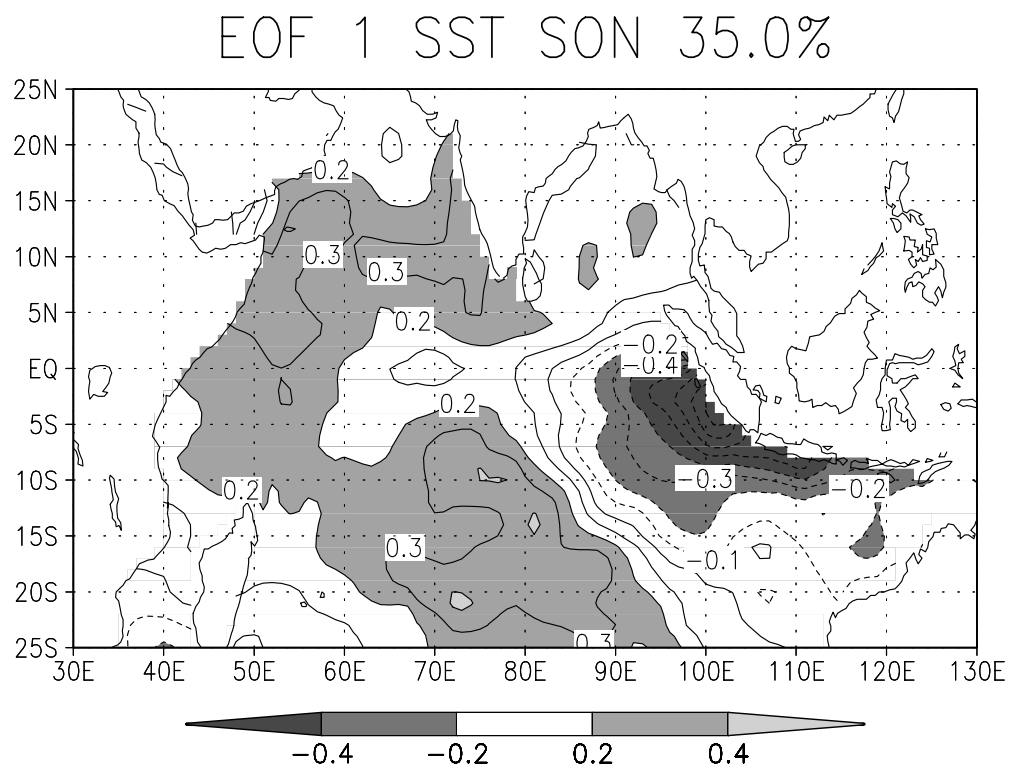


Fig. 1

(b)

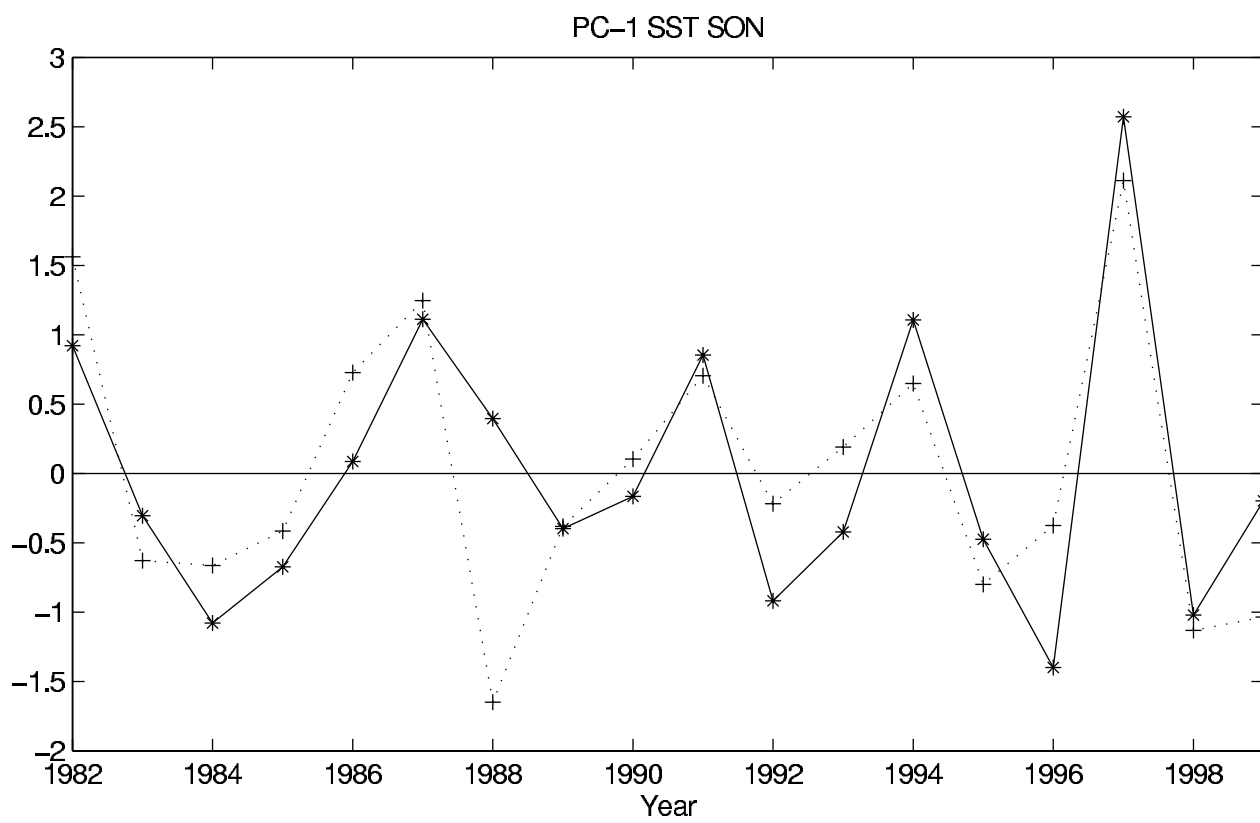


Fig. 2

(a)

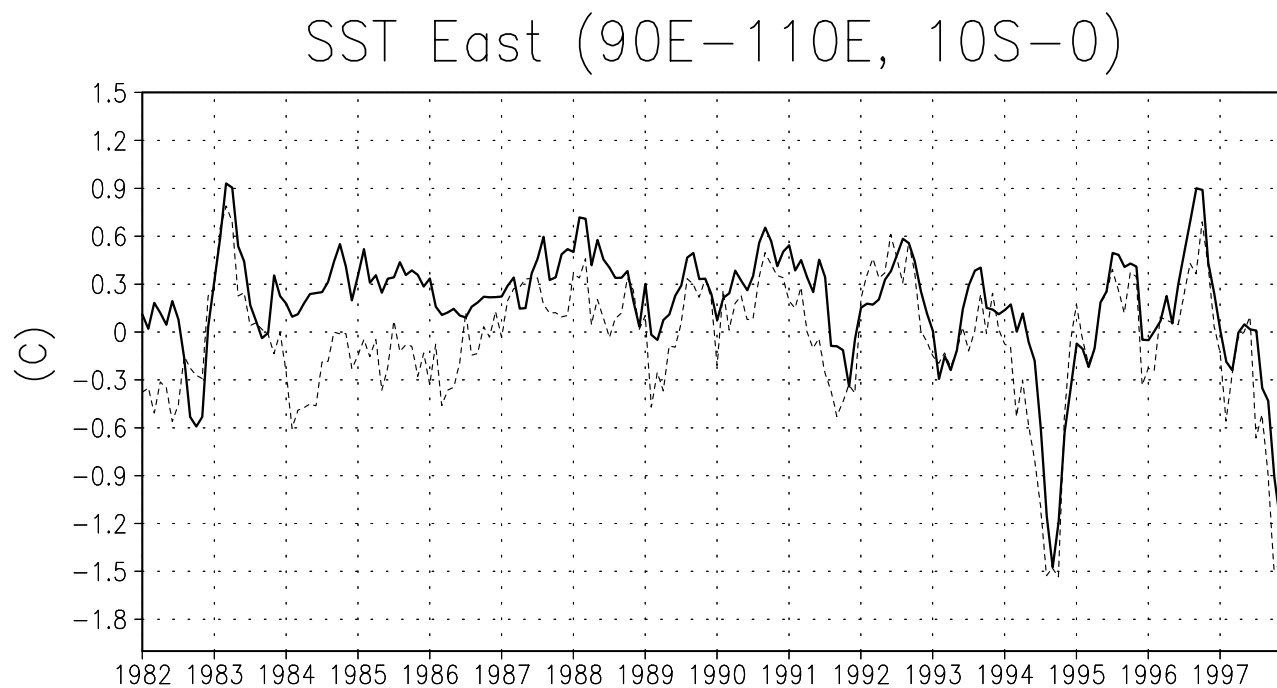
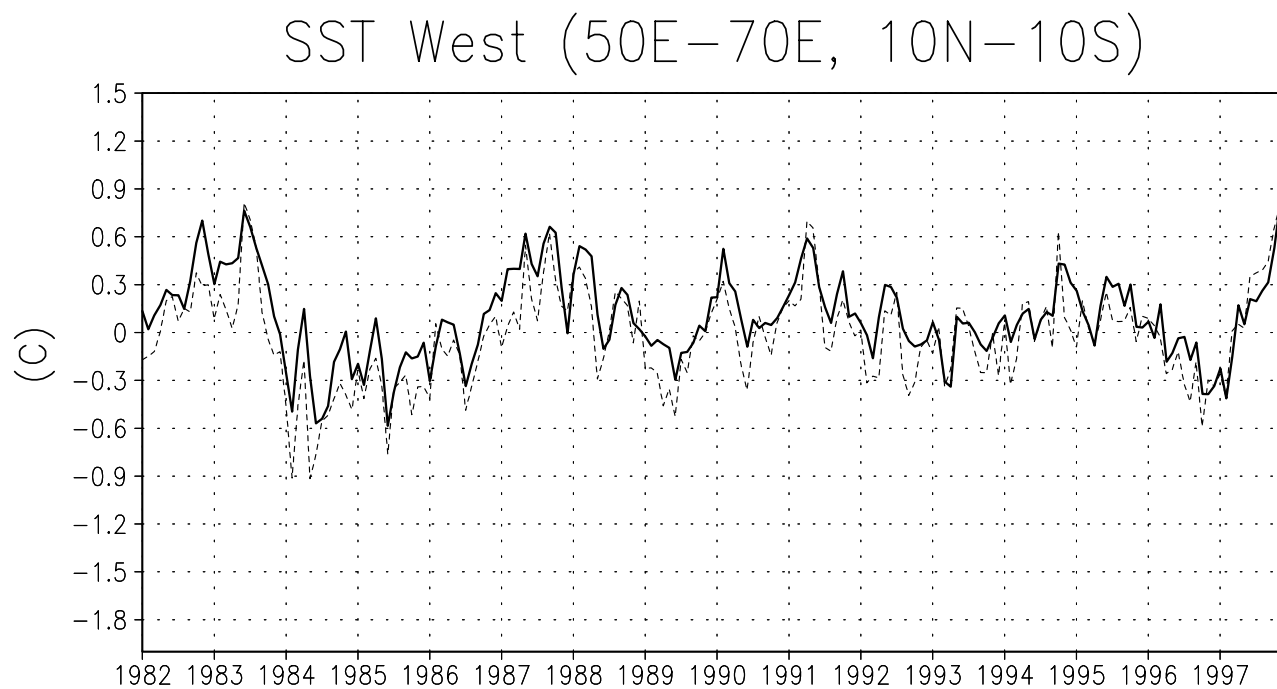


Fig. 2

(b)

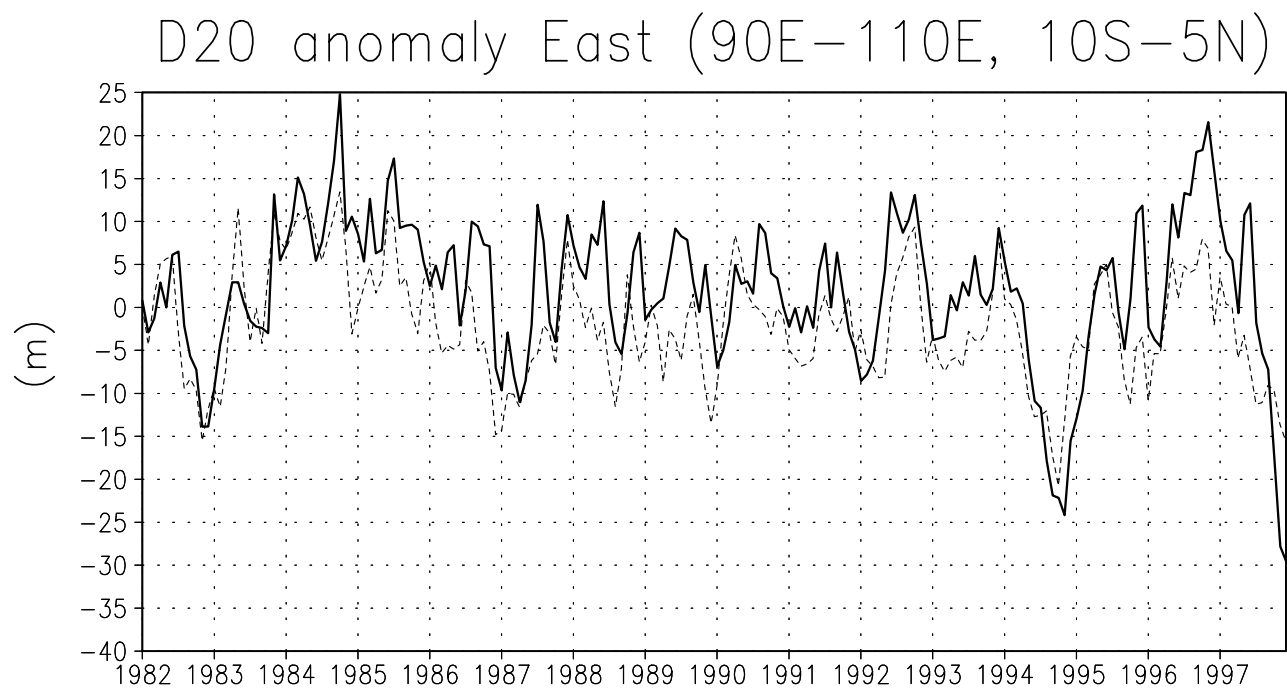
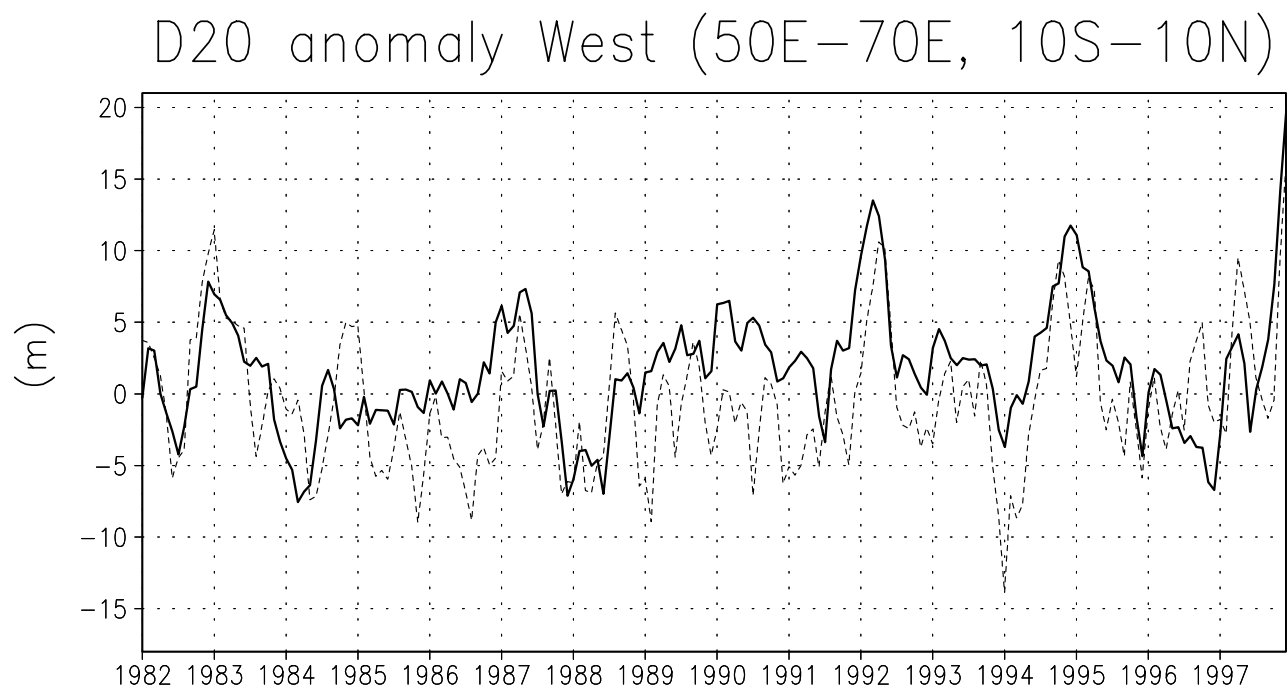


Fig. 3

(a)

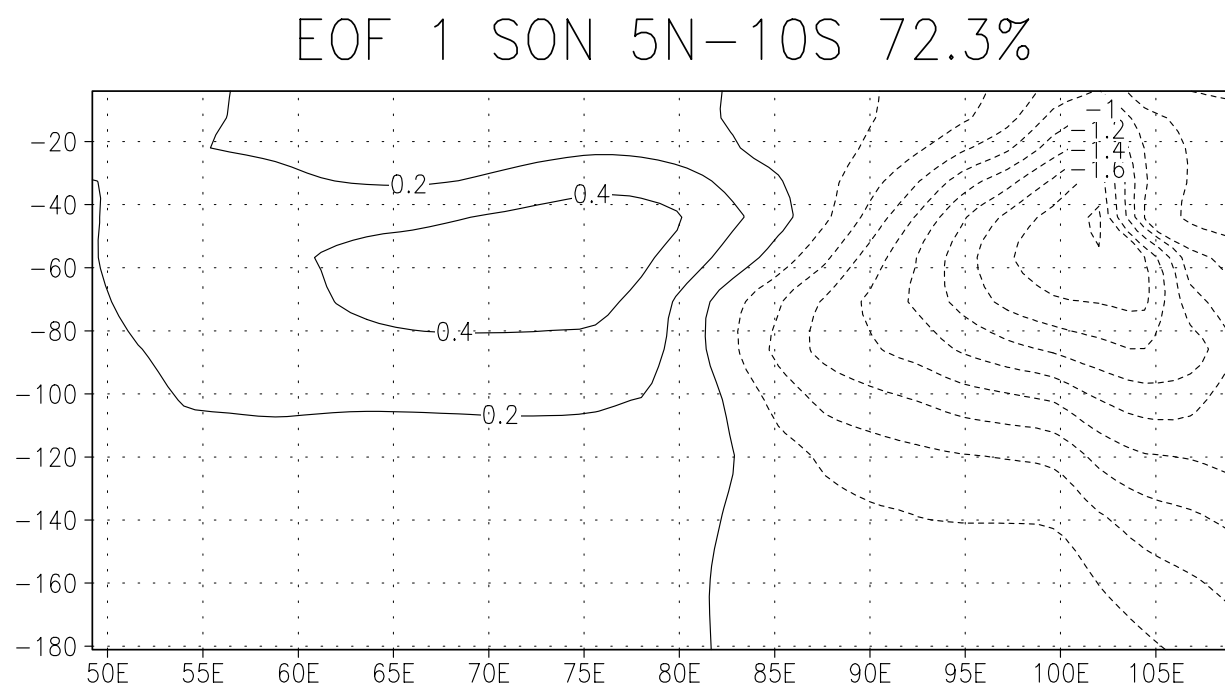


Fig. 3

(b) PC-1 SON 5N-10S

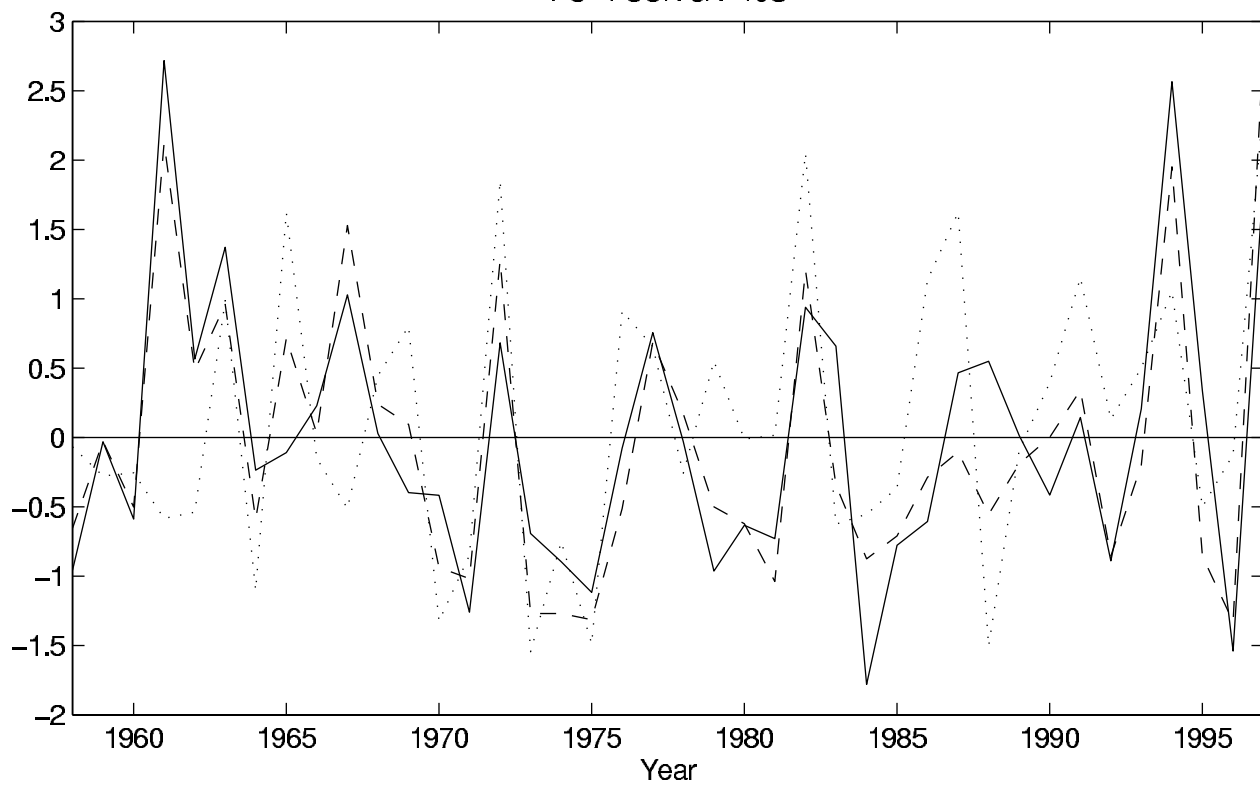




Fig. 4

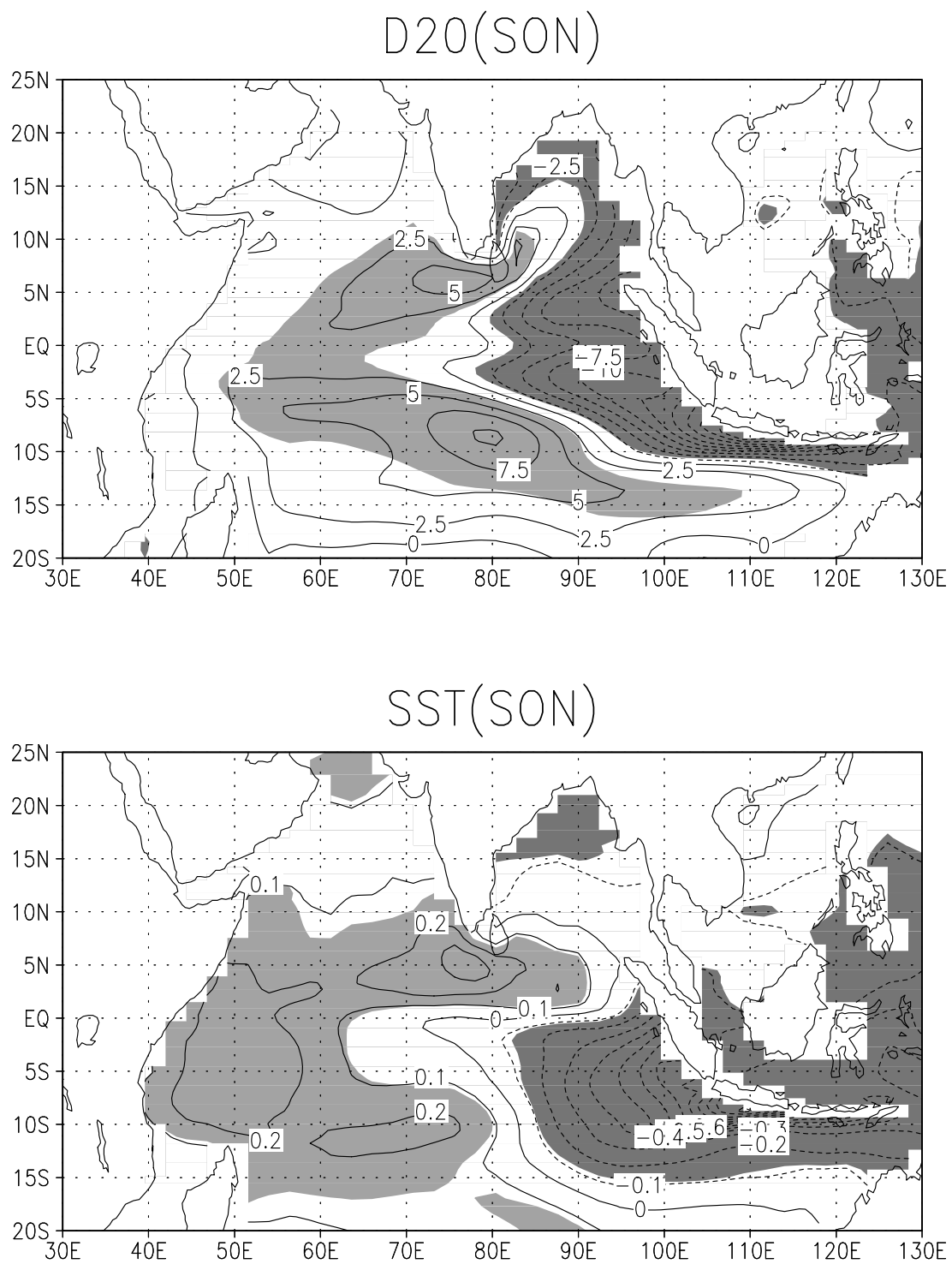


Fig. 5

(a)

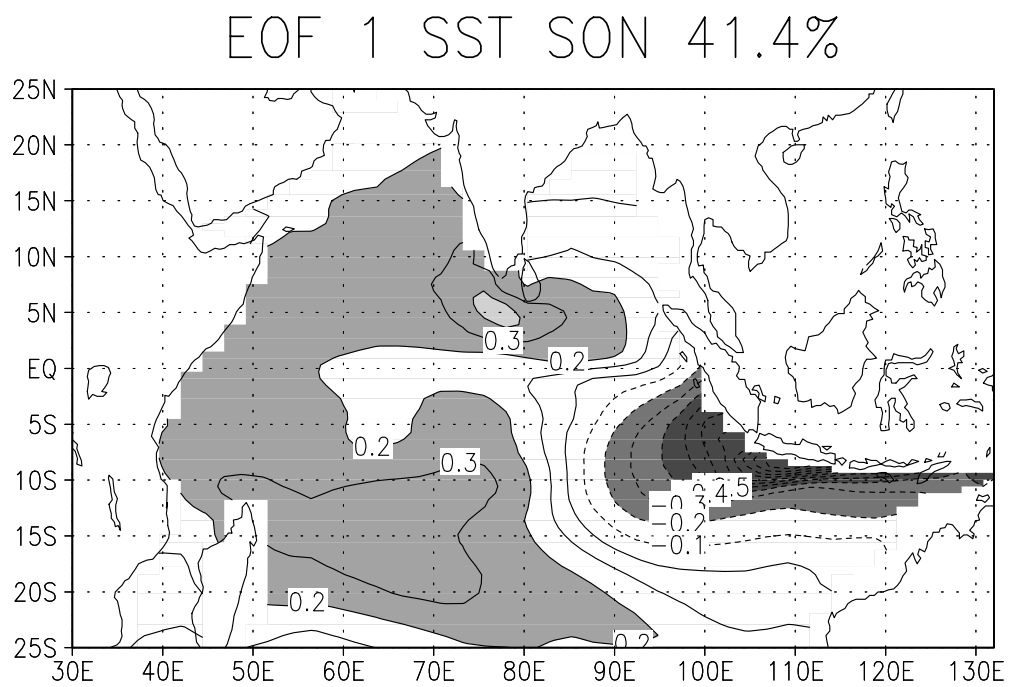


Fig. 5

(b)

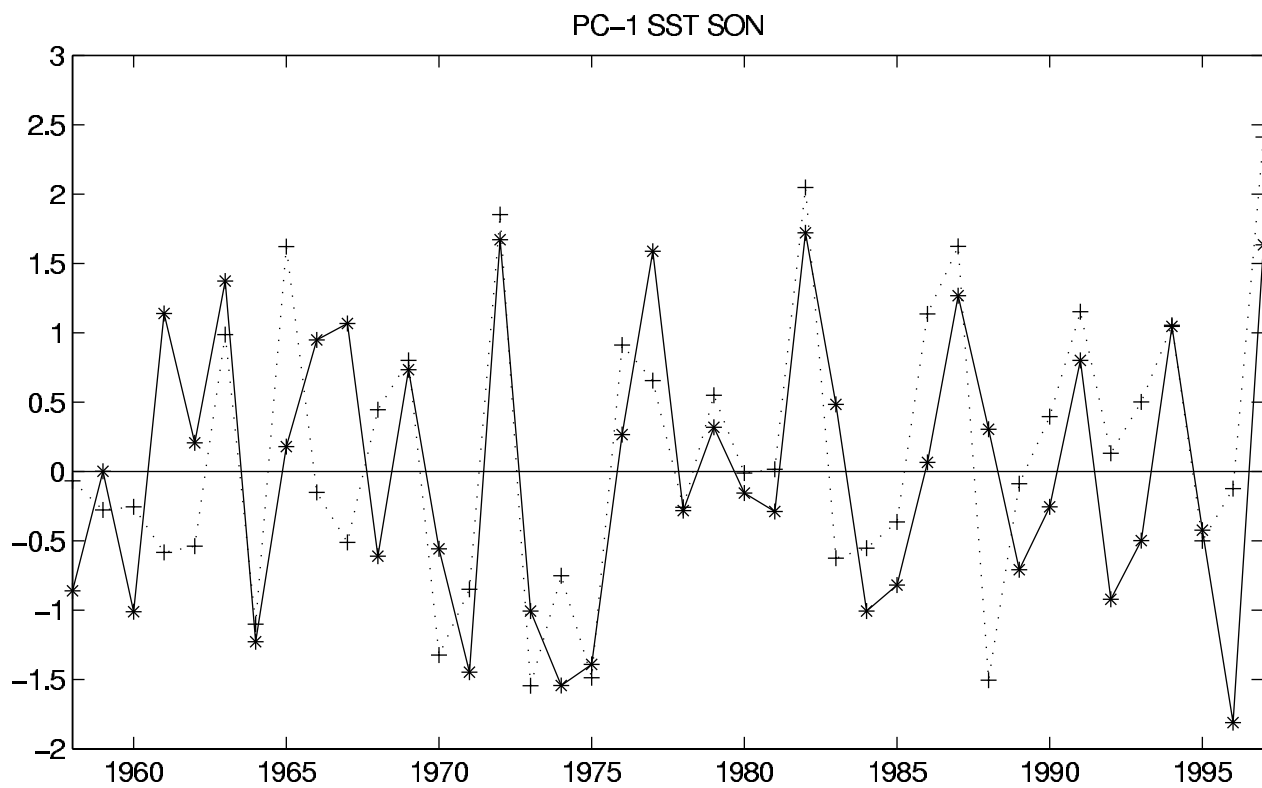
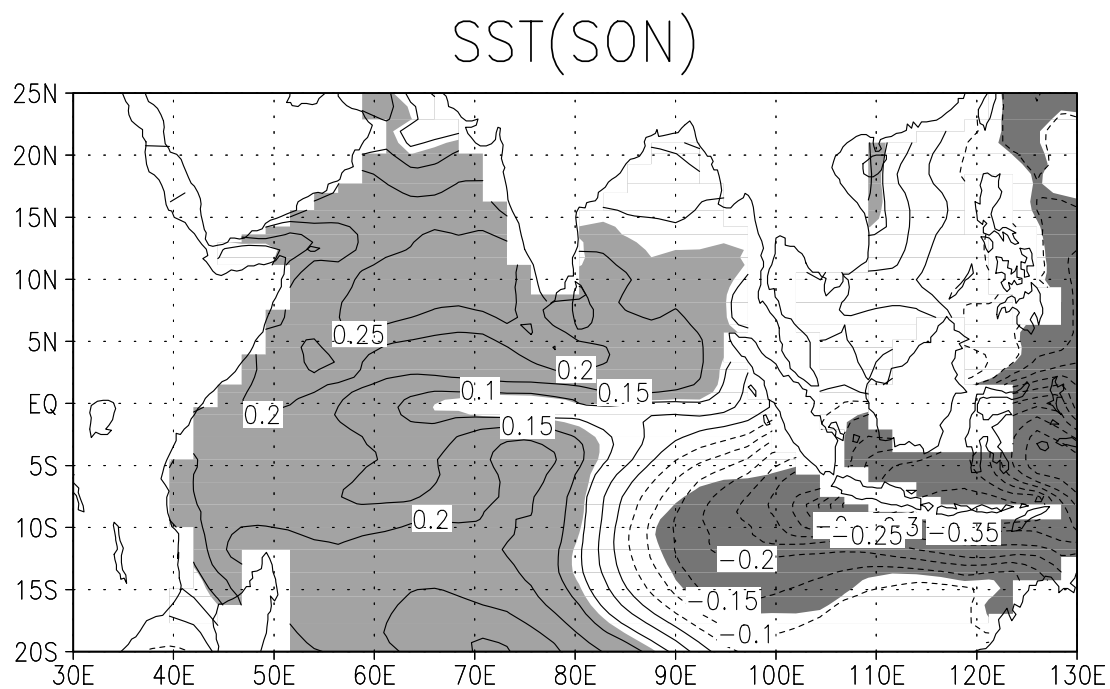


Fig. 6

(a)



(b)

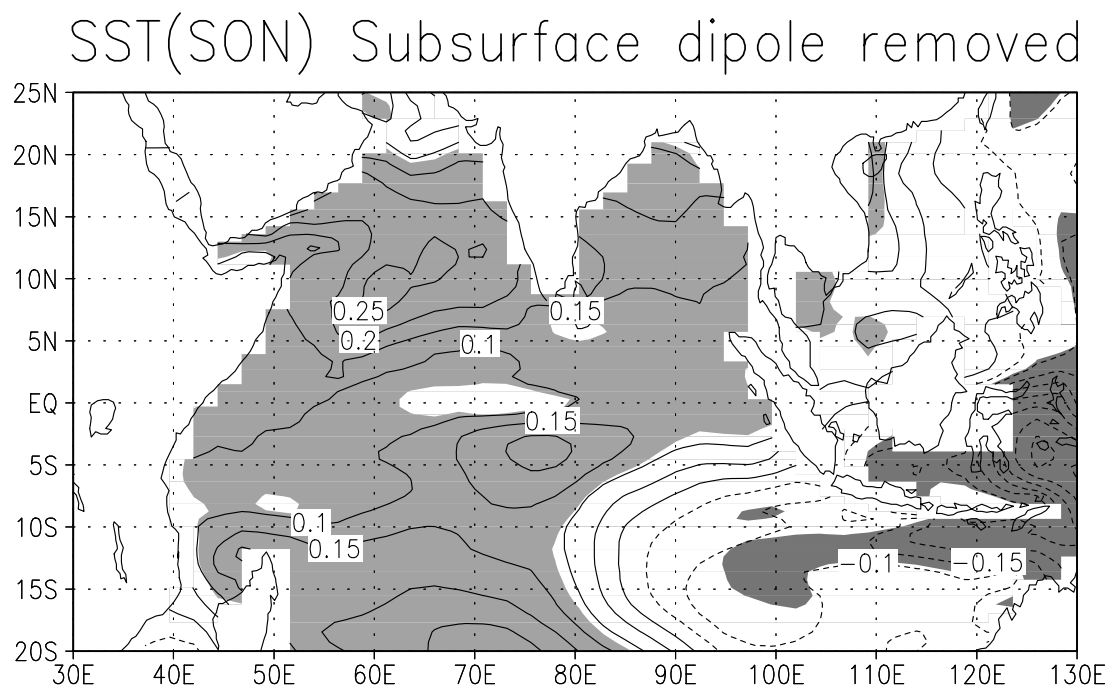
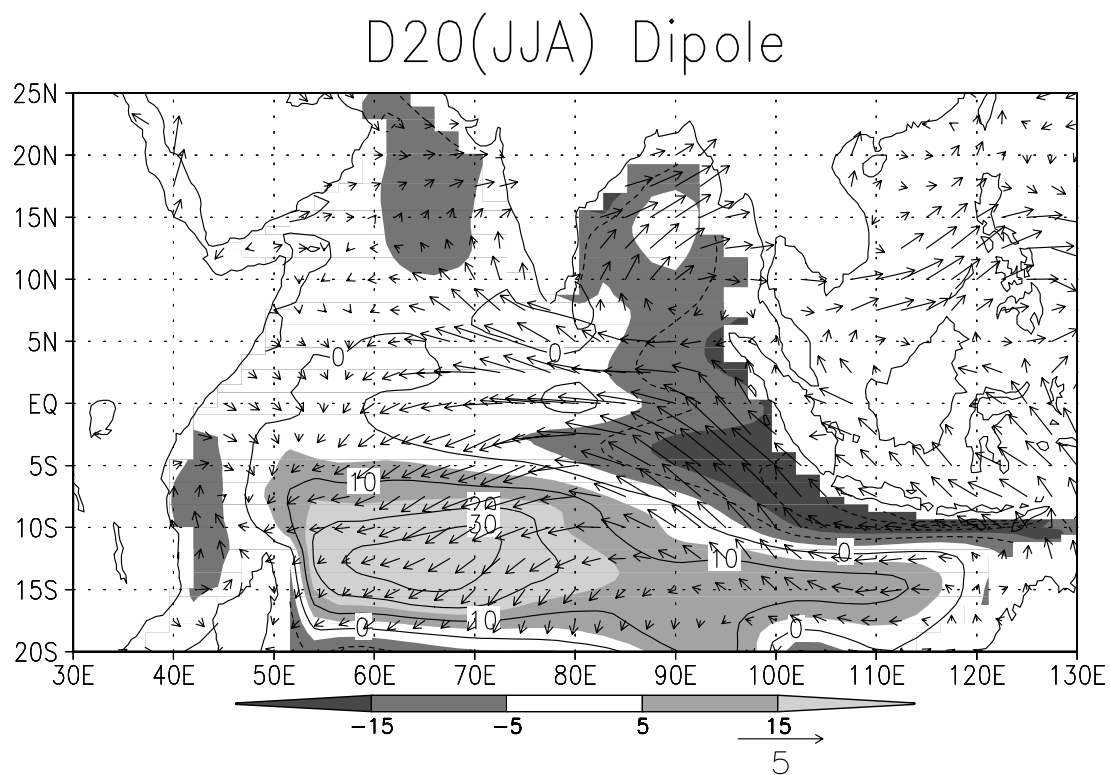


Fig. 7

(a)



(b)

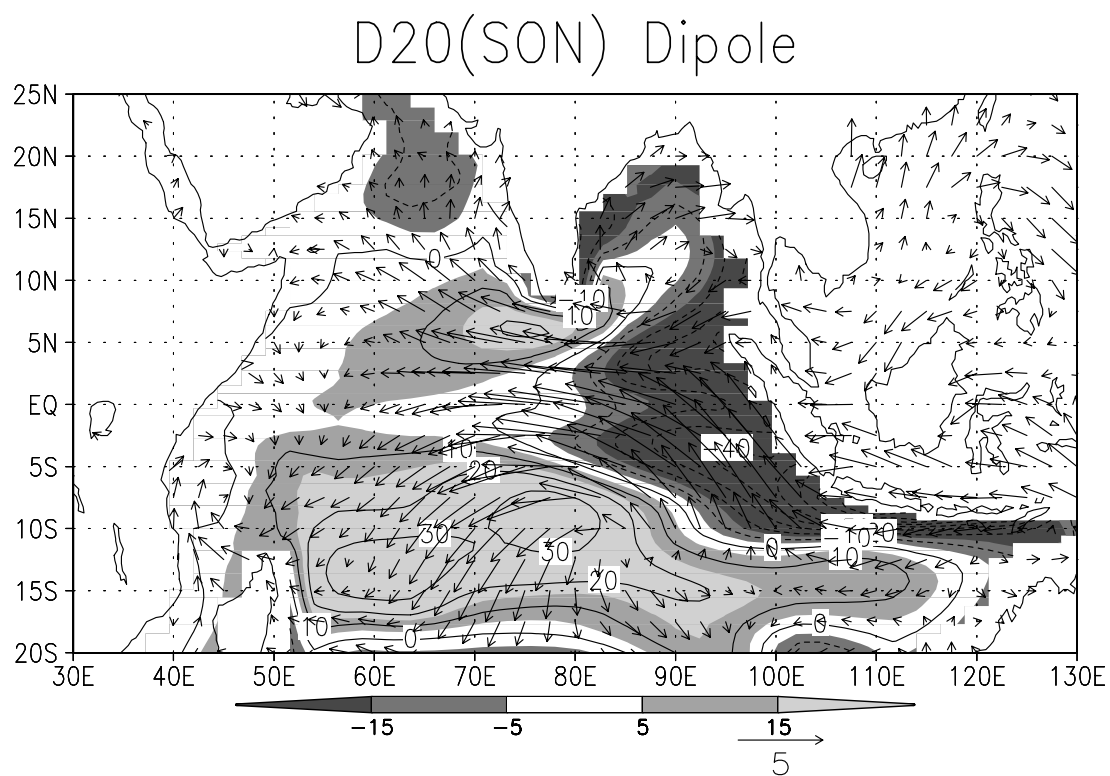
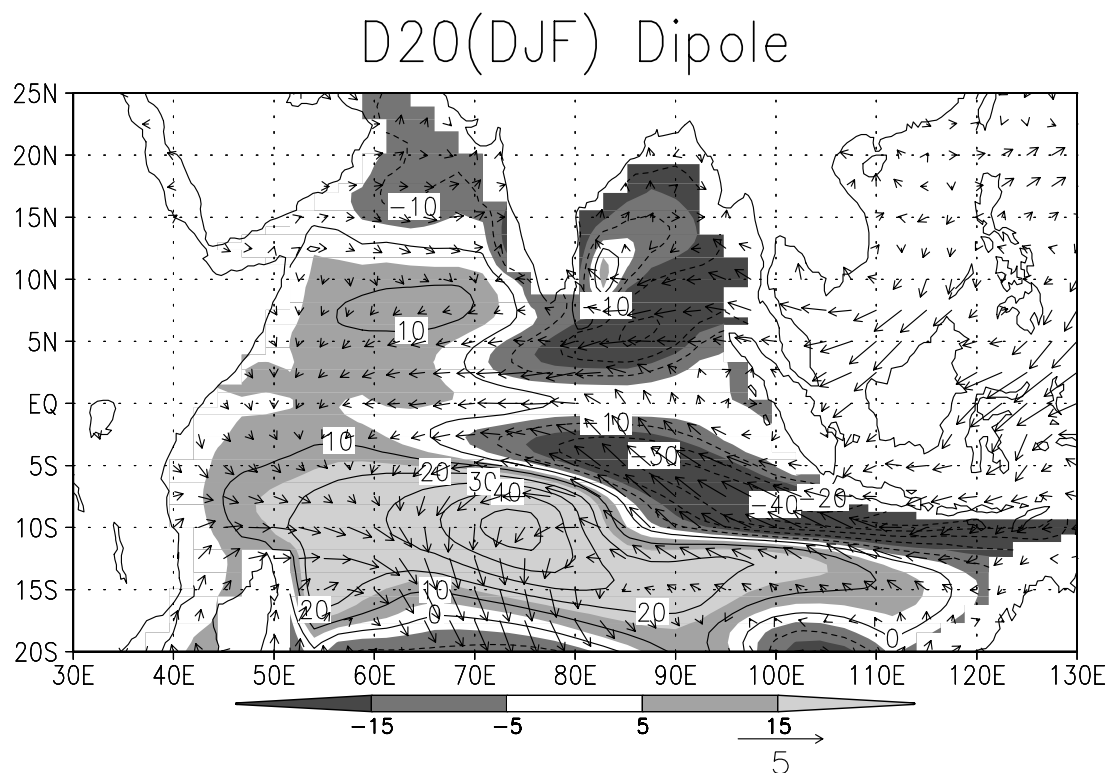


Fig. 7

(c)



(d)

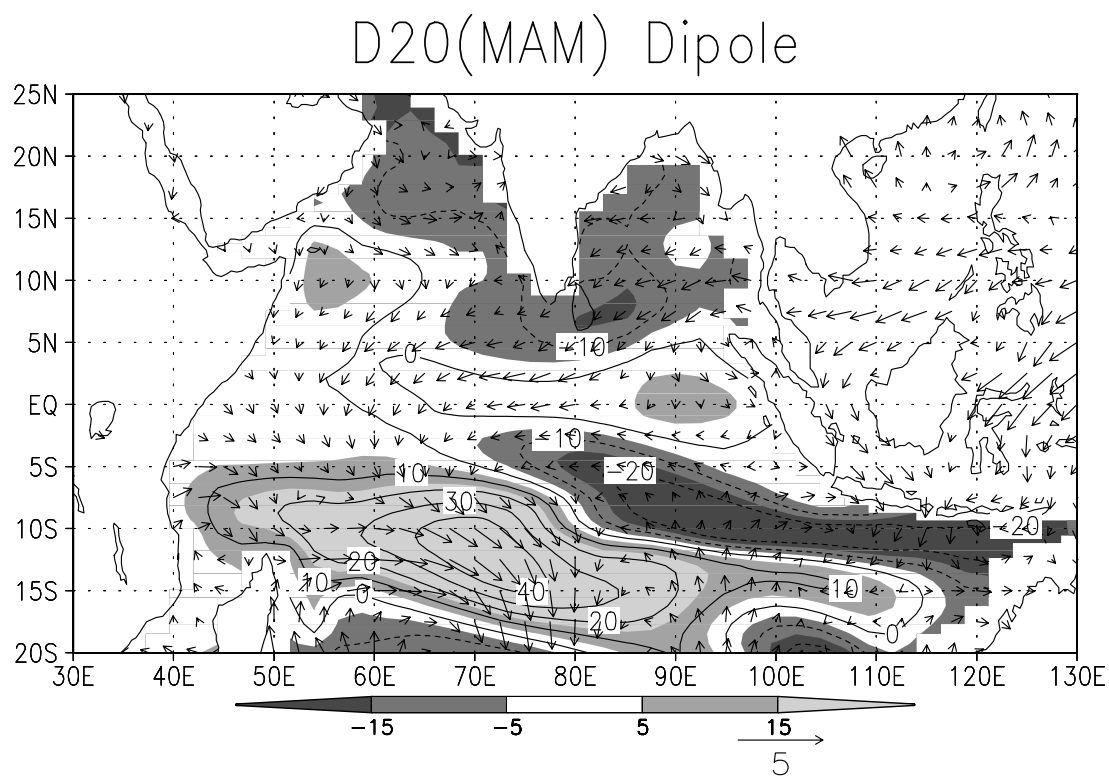
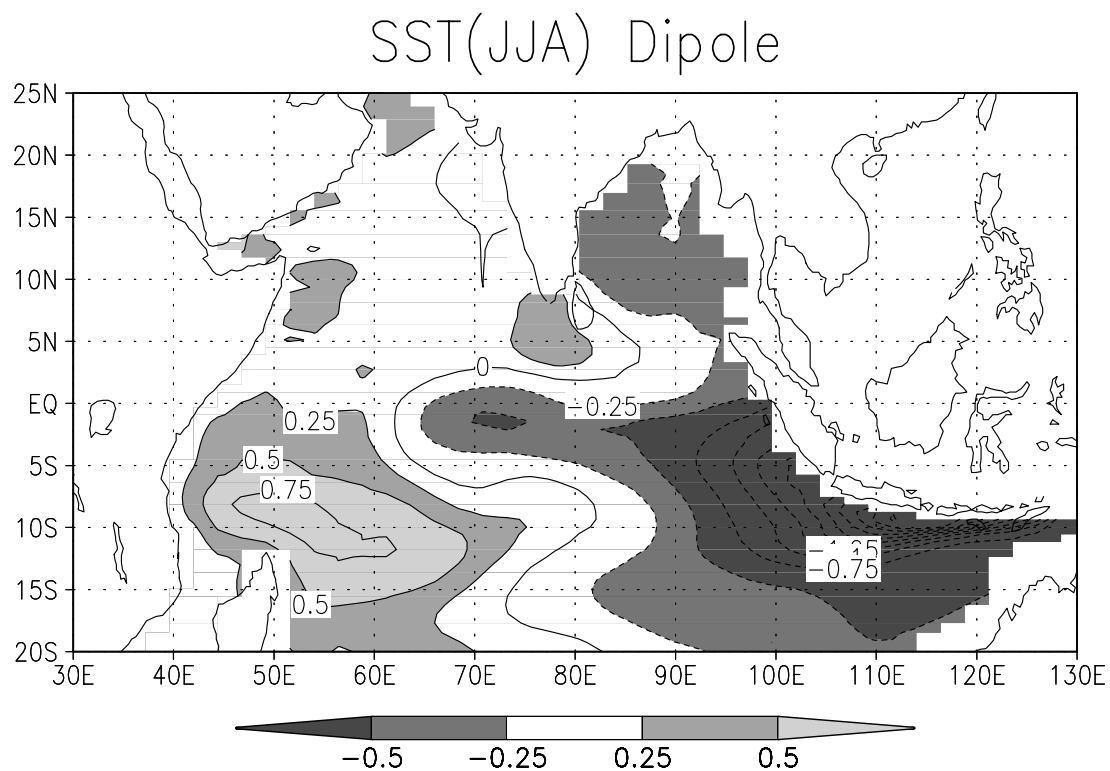


Fig. 8

(a)



(b)

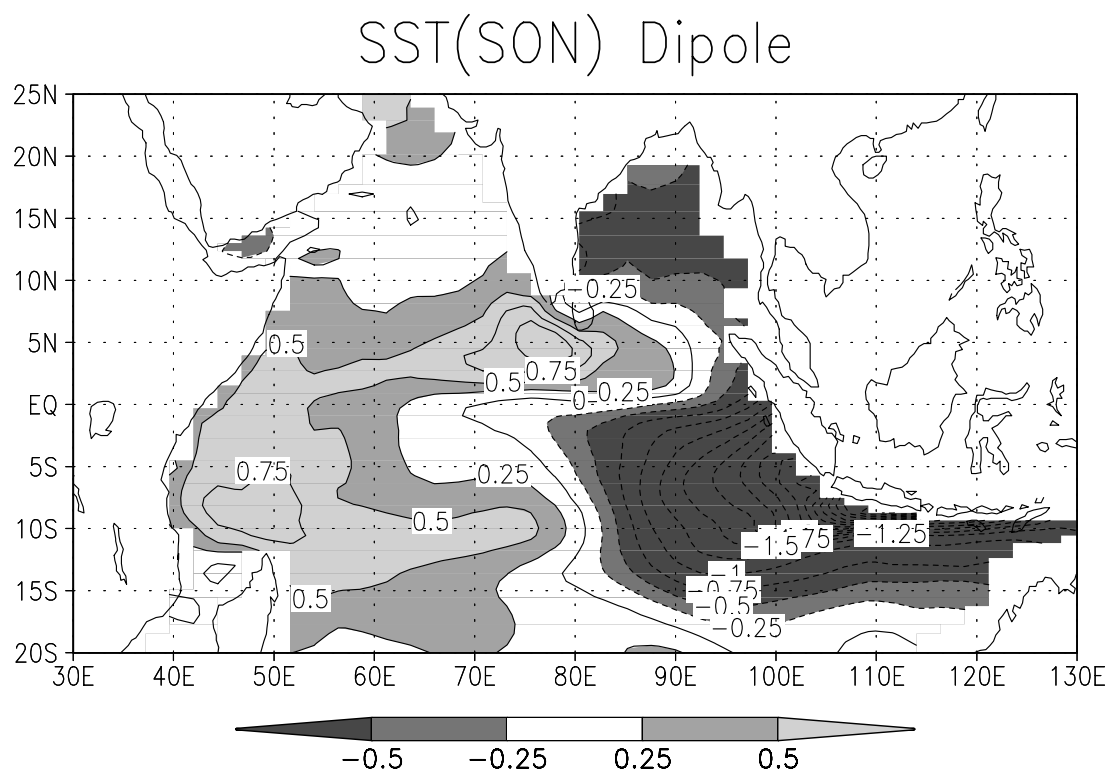
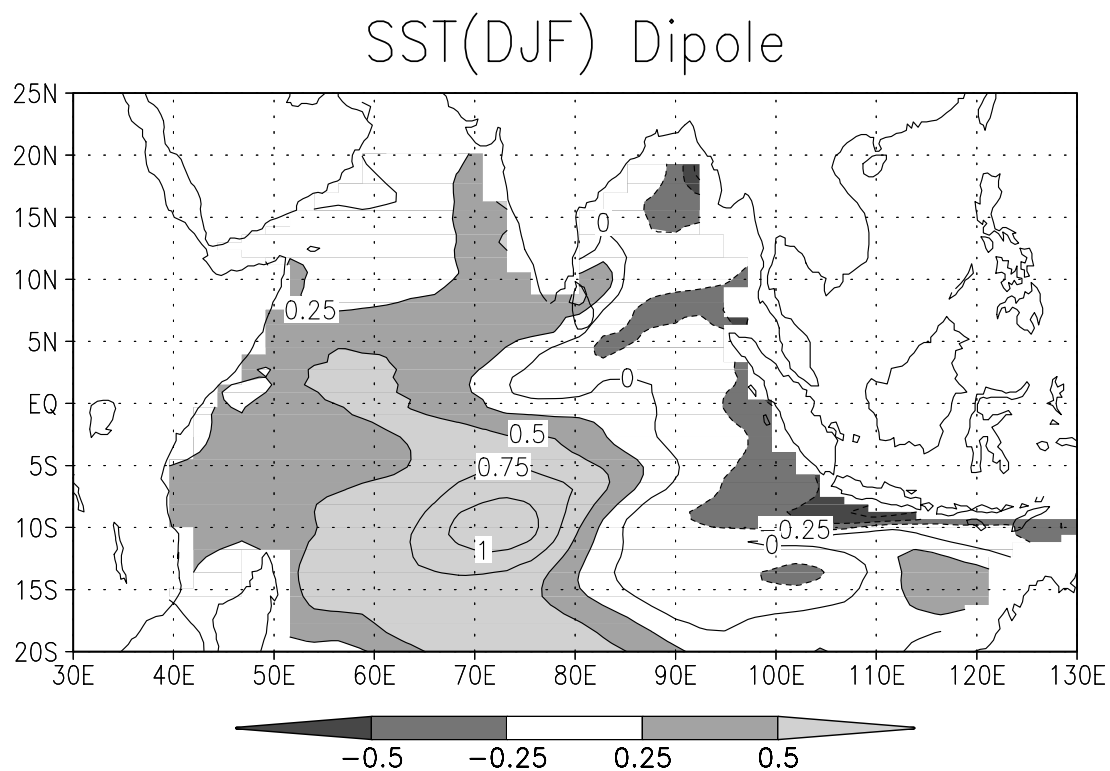


Fig. 8

(c)



(d)

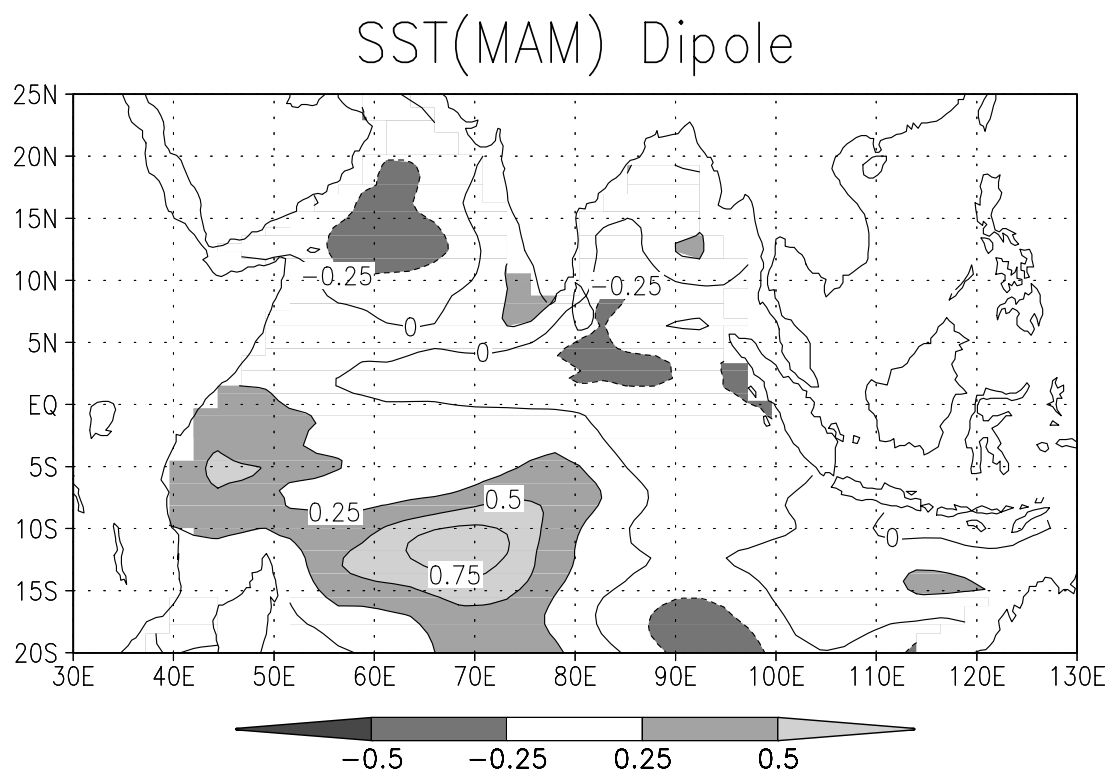
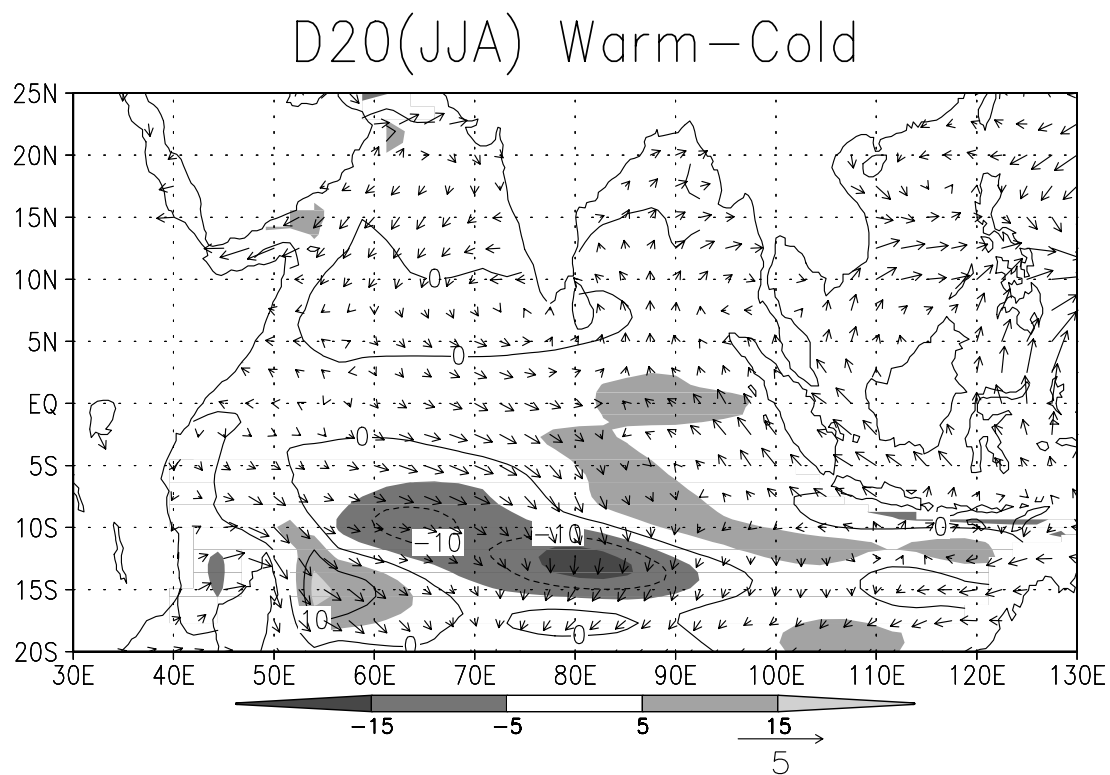




Fig. 9

(a)



(b)

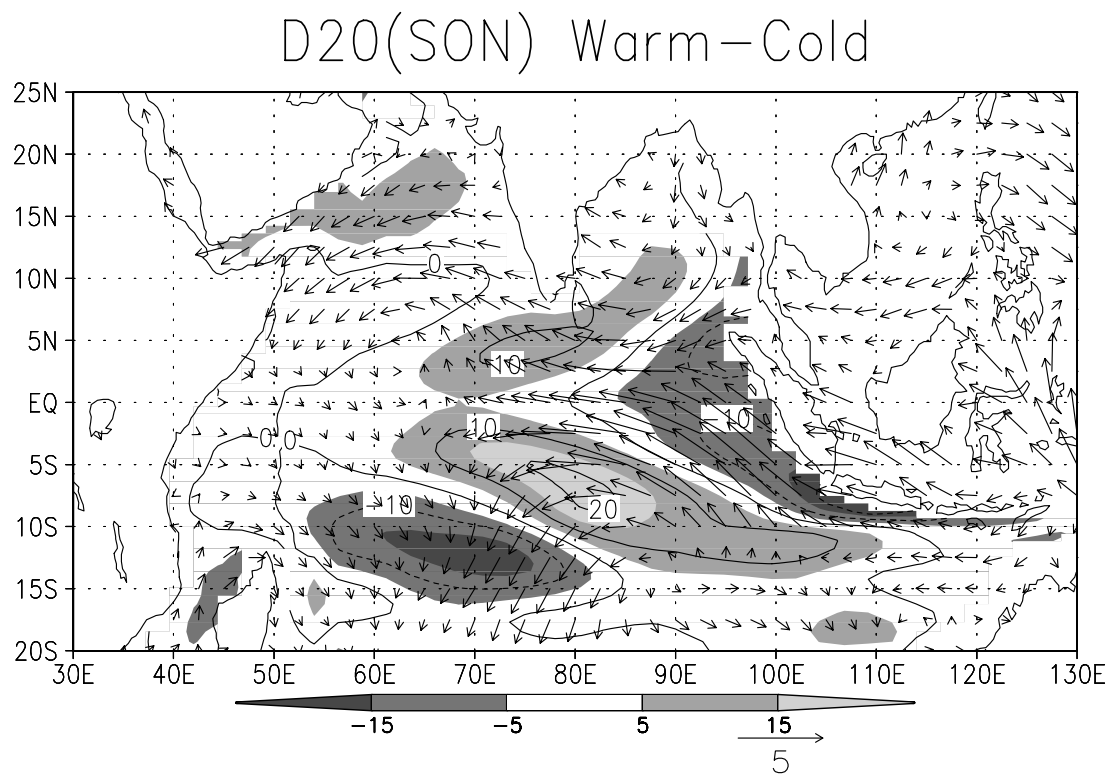
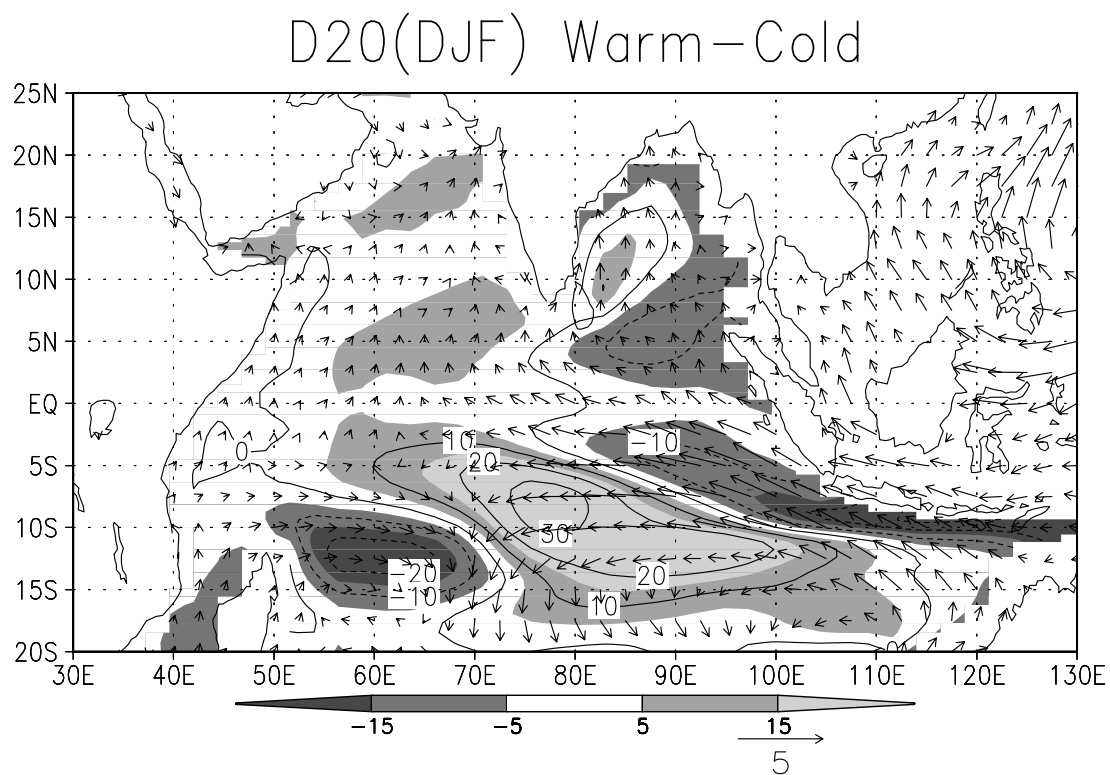


Fig. 9

(c)



(d)

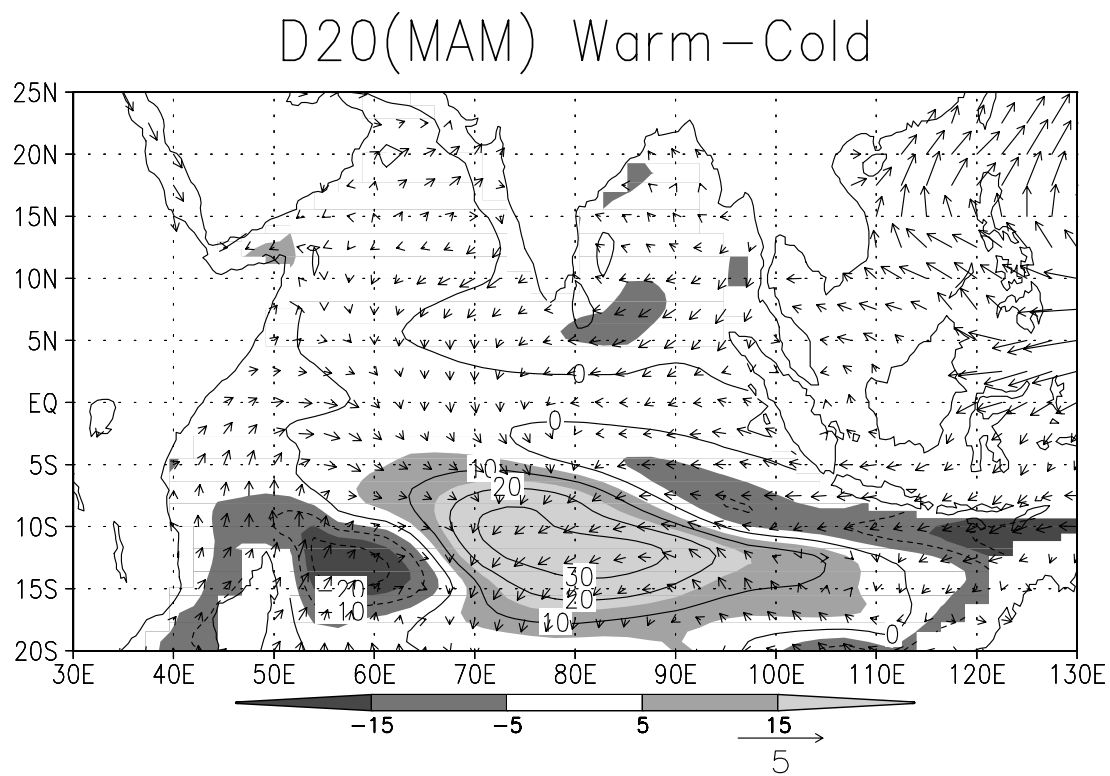
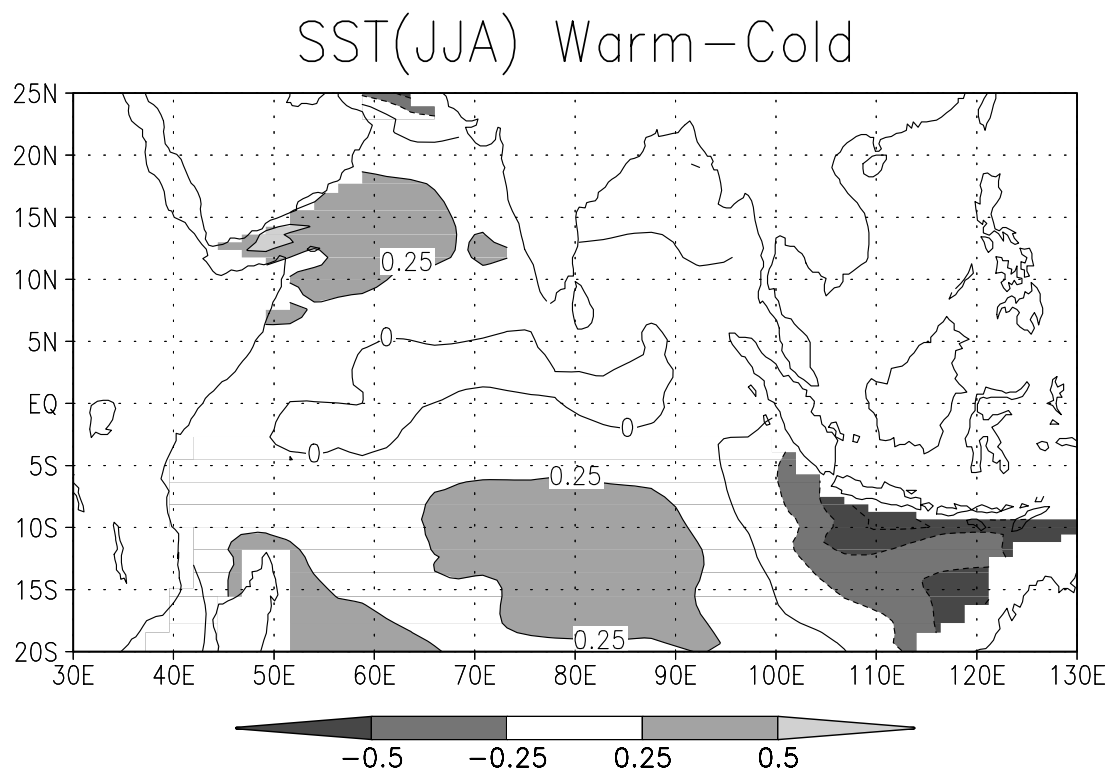


Fig. 10

(a)



(b)

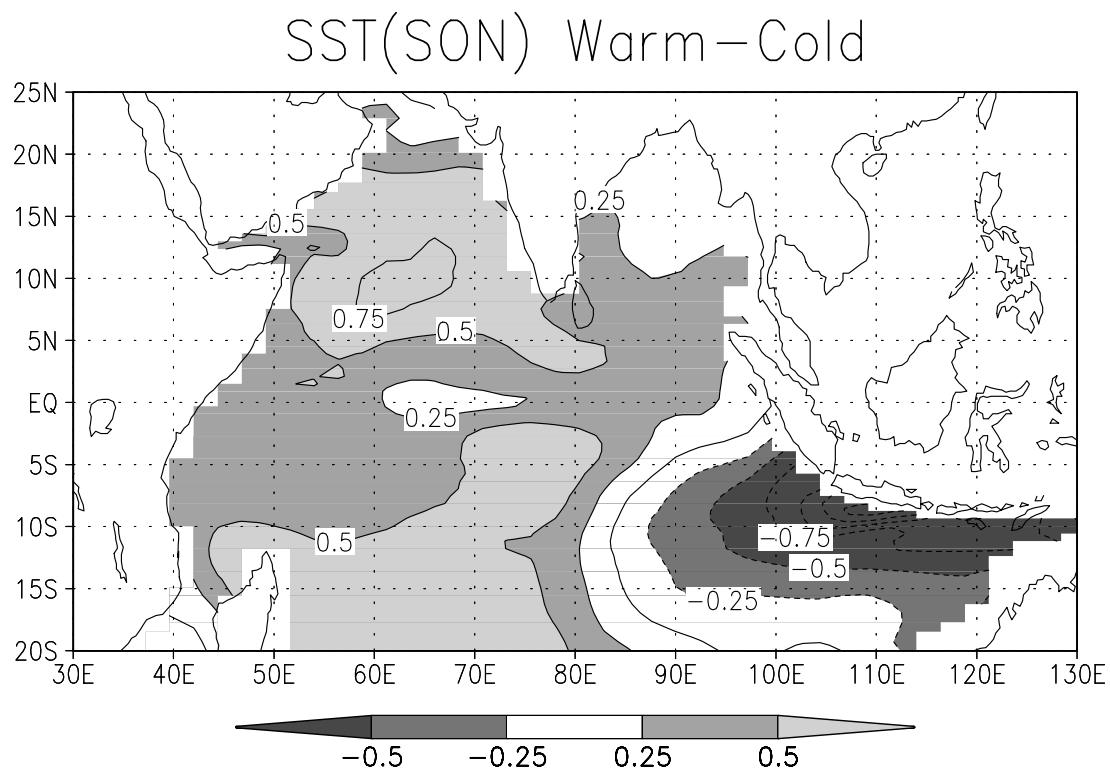
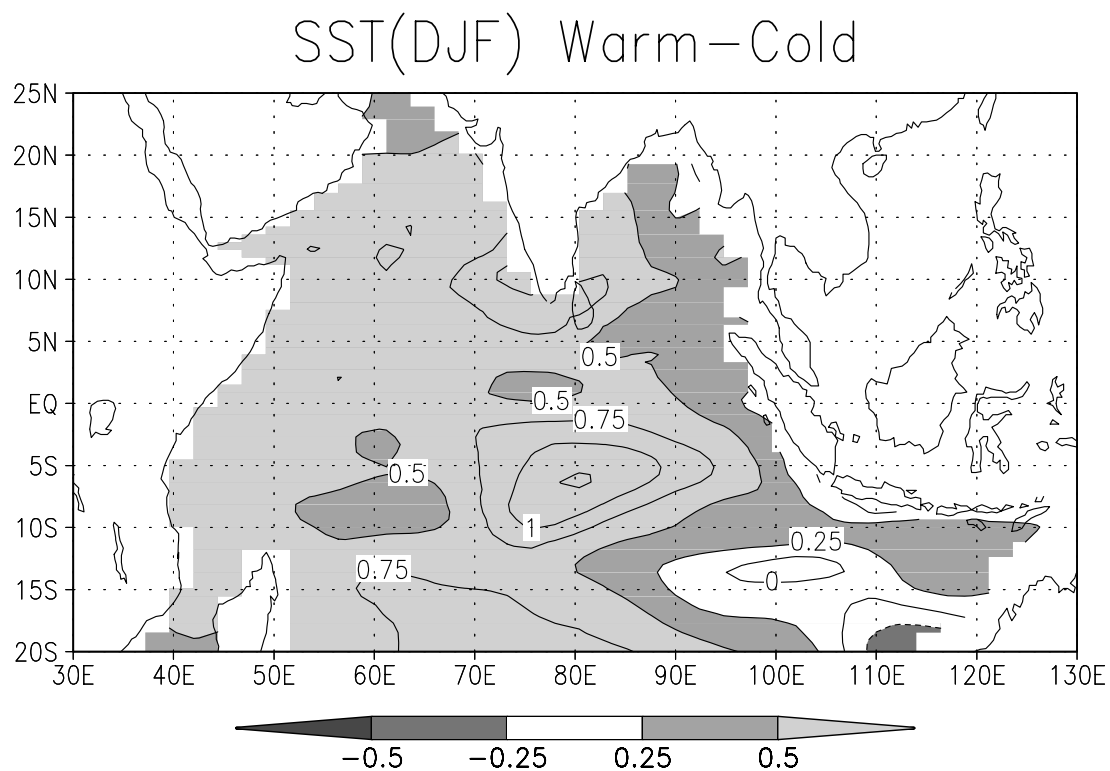


Fig. 10

(c)



(d)

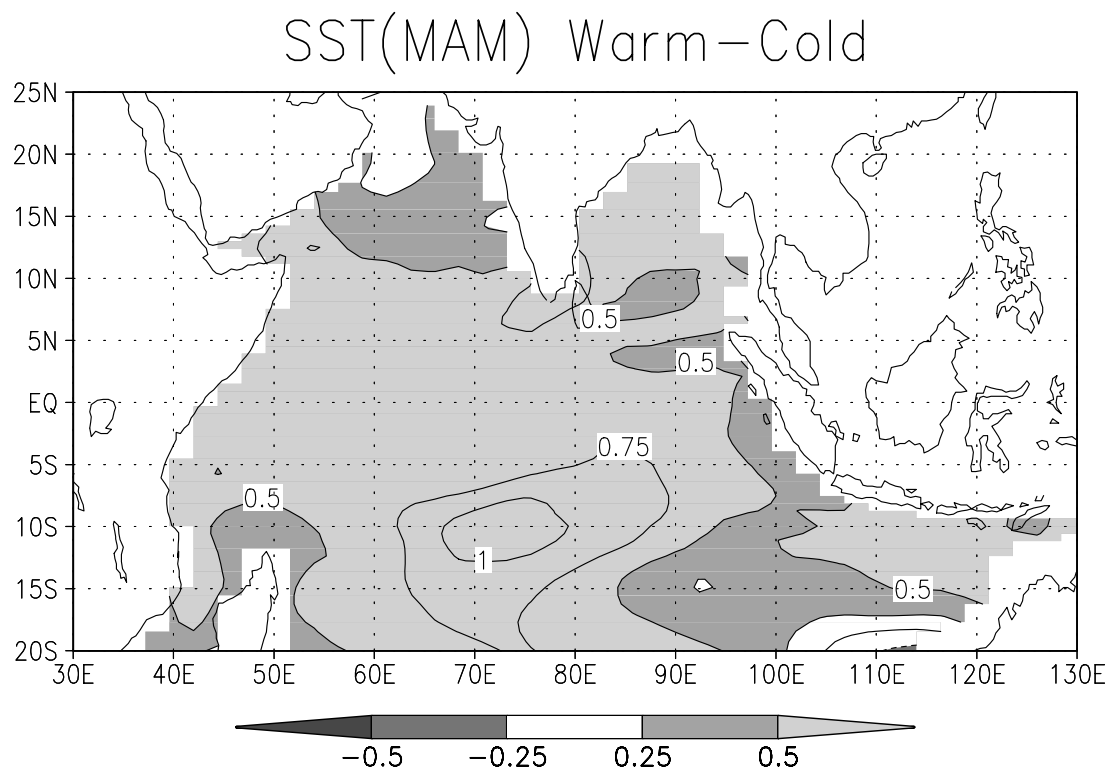


Fig. 11

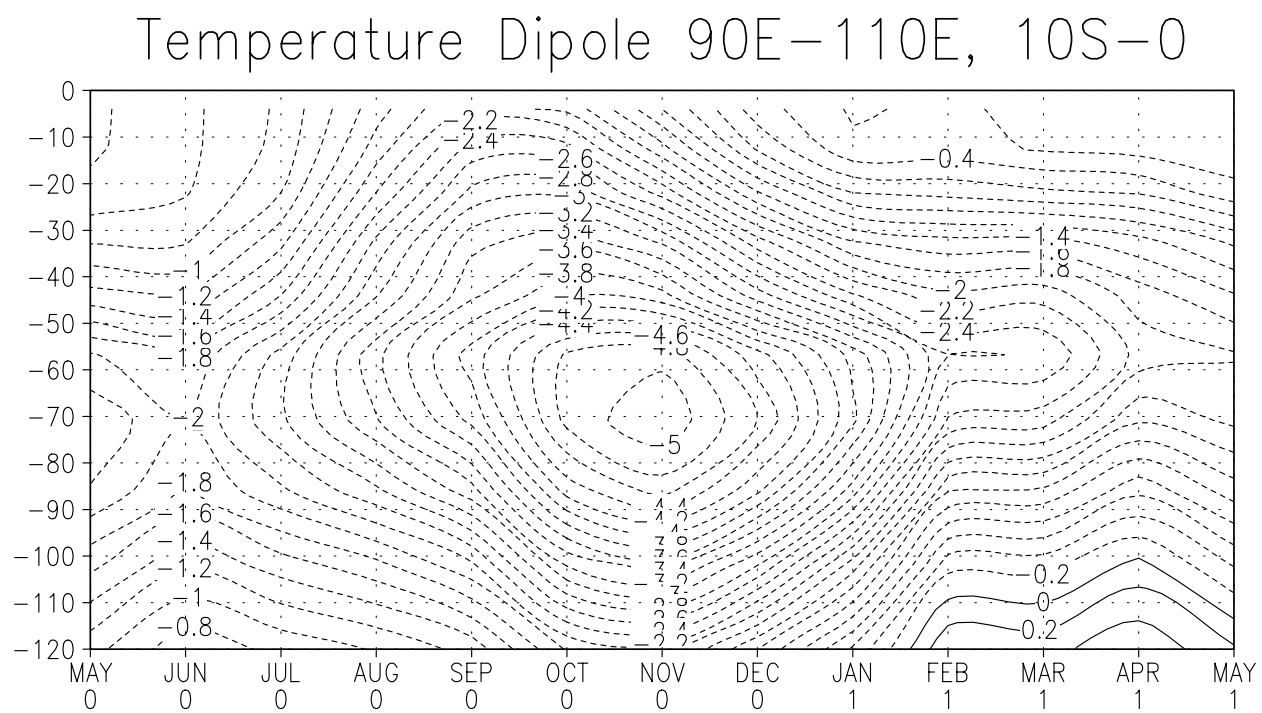
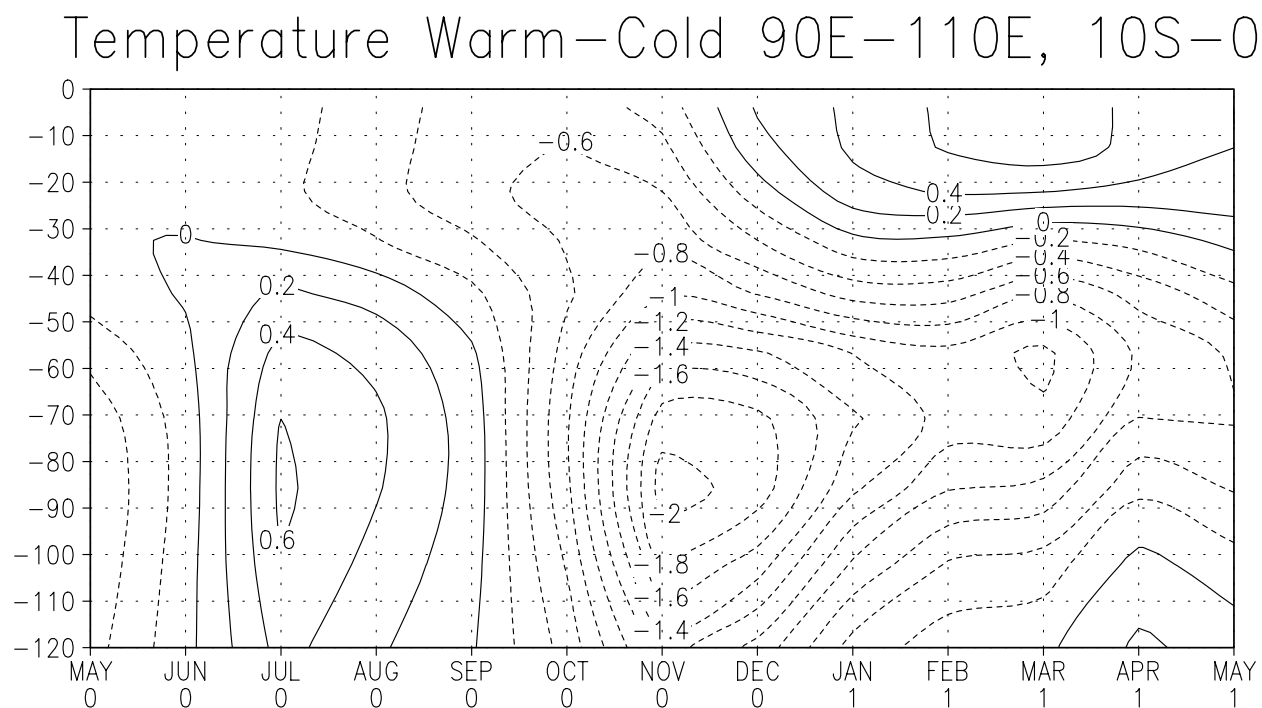


Fig. 12

(a)

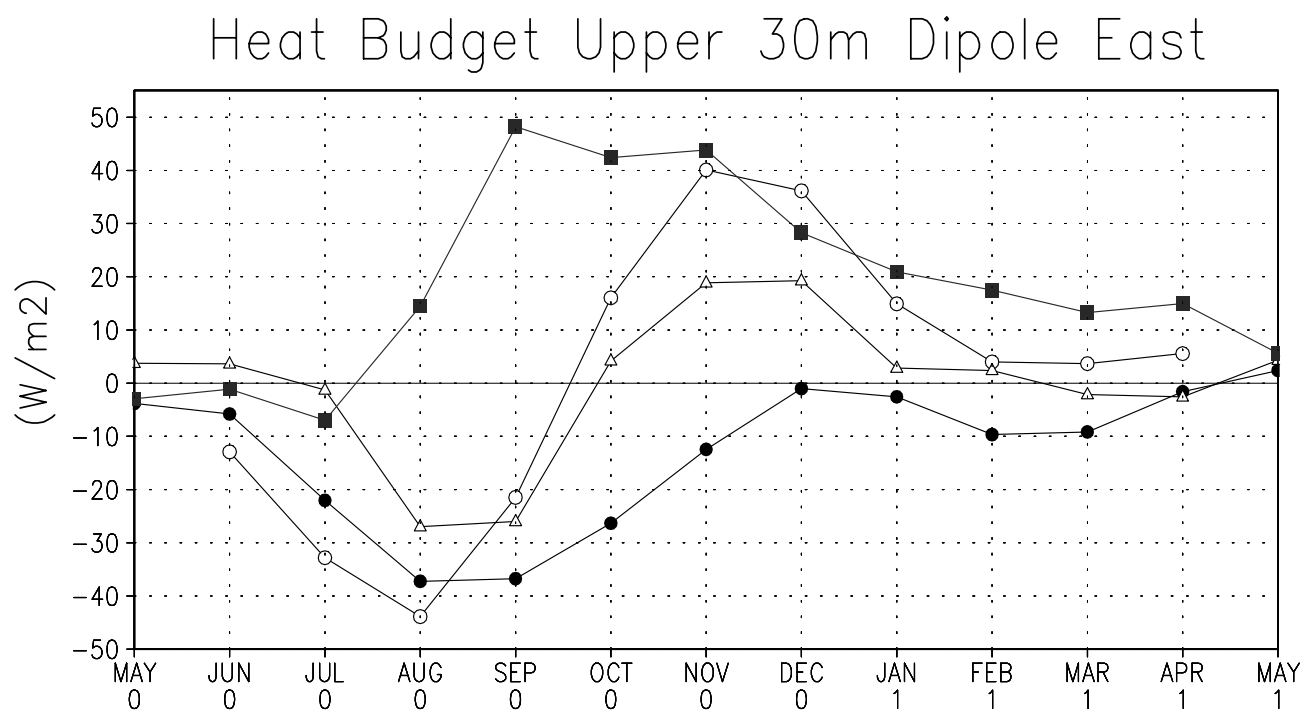
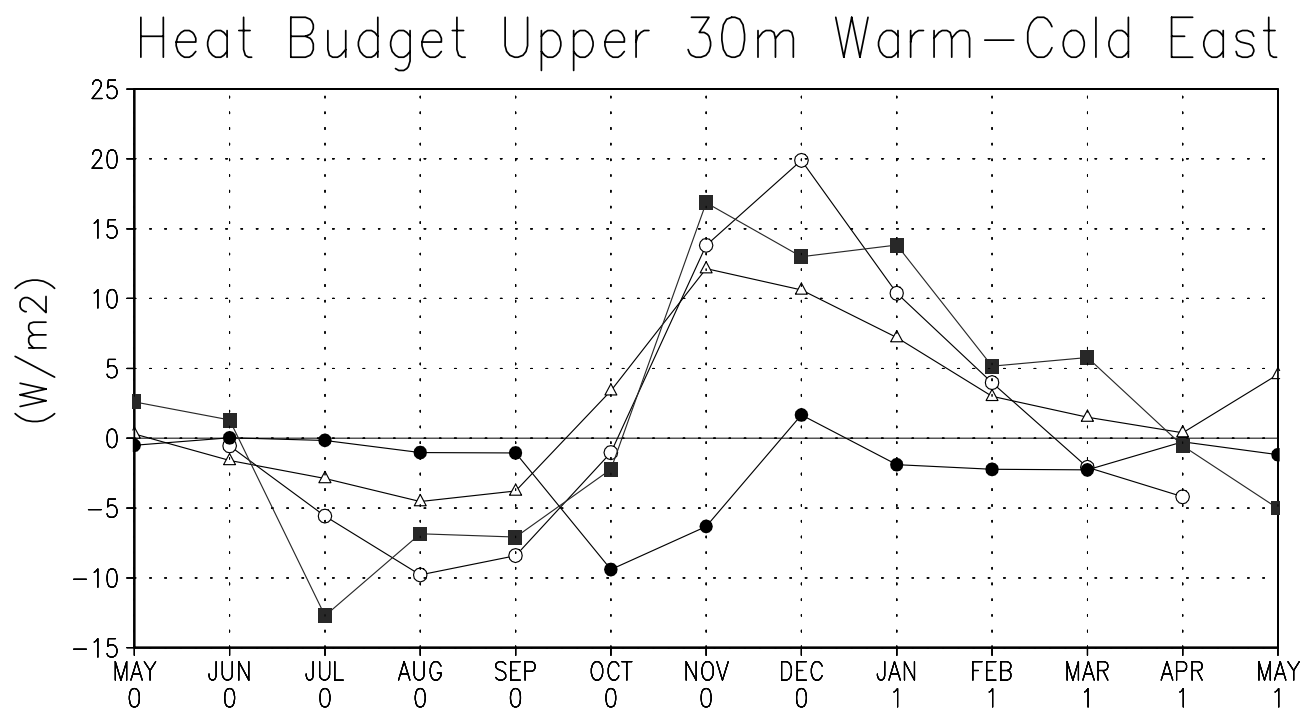


Fig. 12

(b)

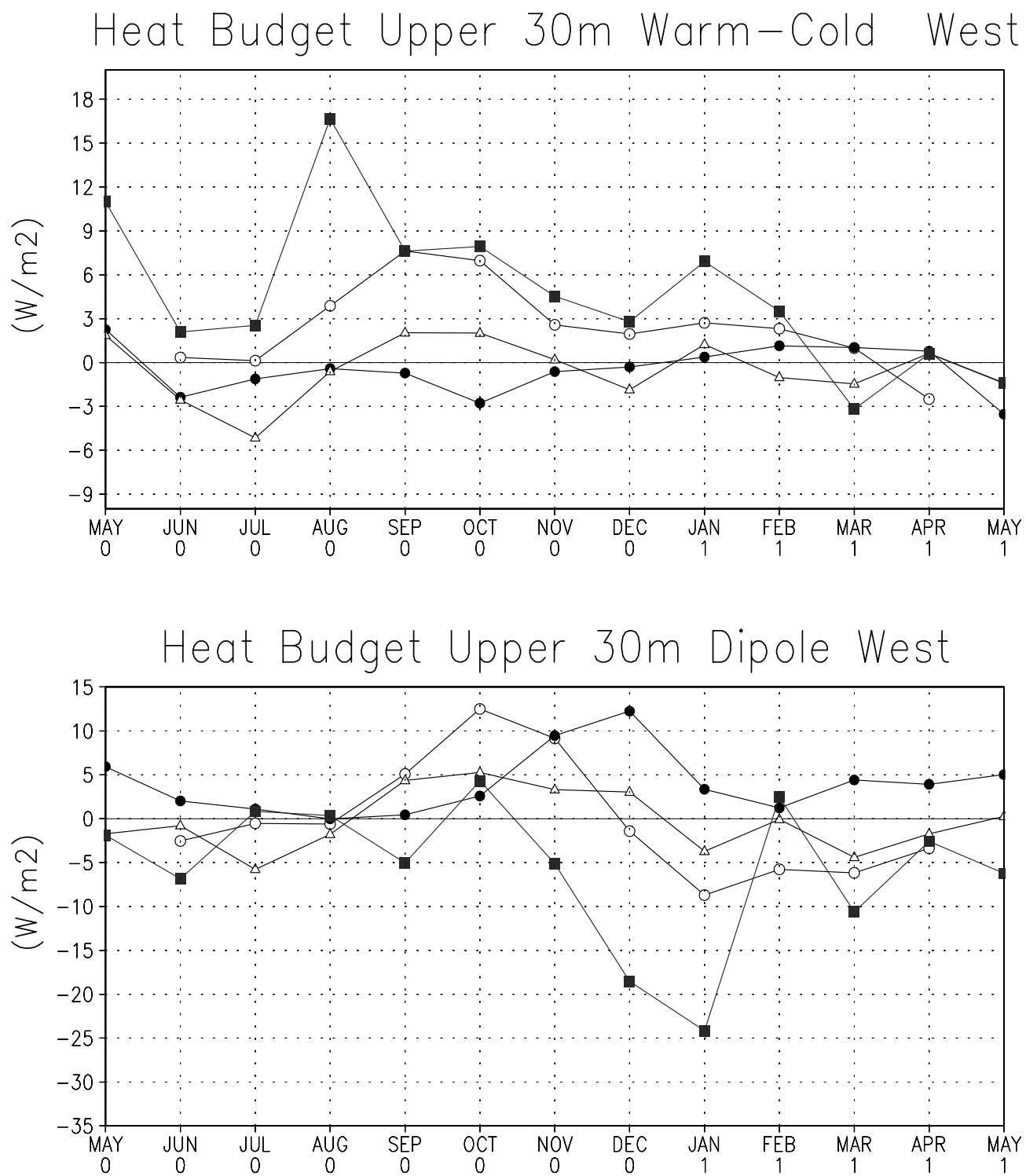
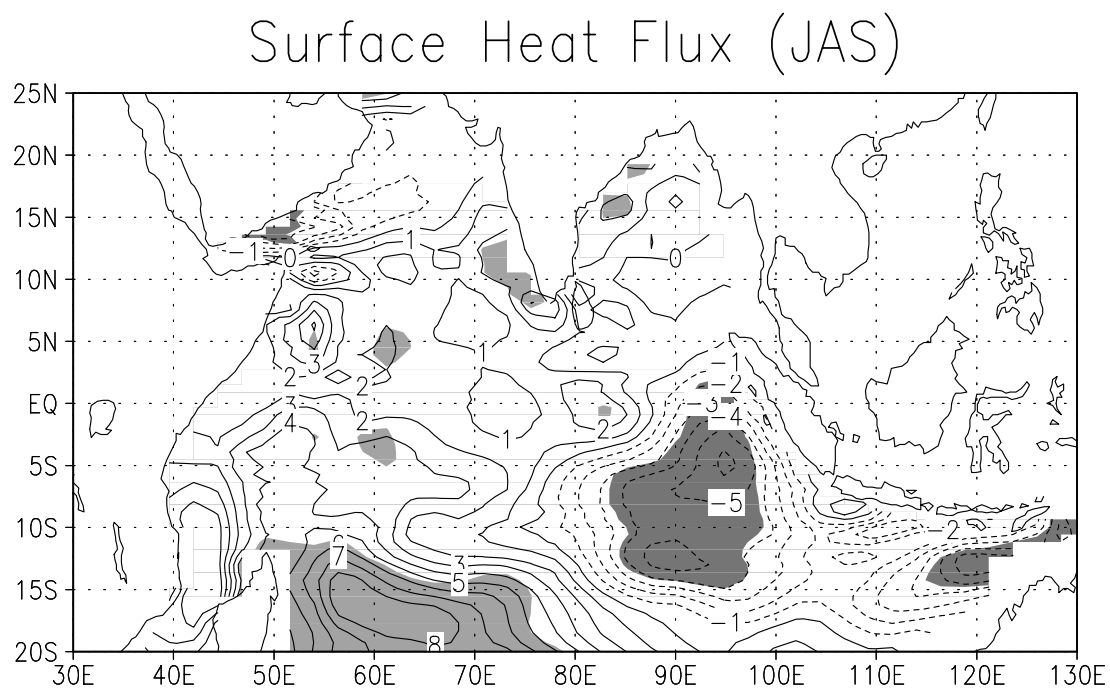


Fig. 13

(a)



(b)

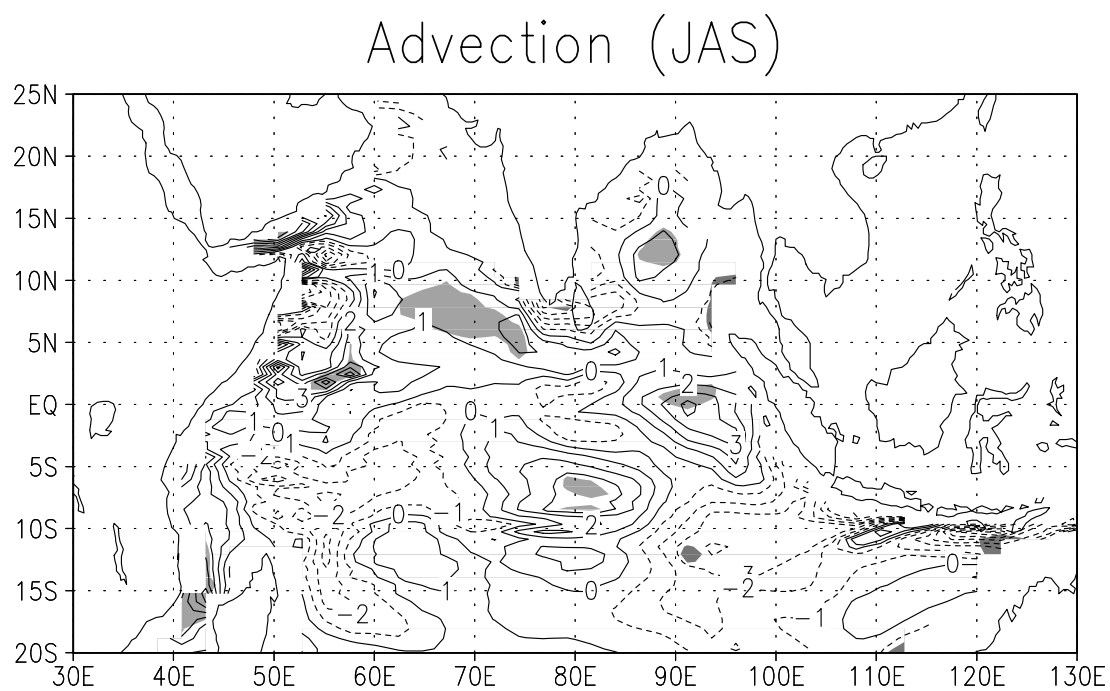
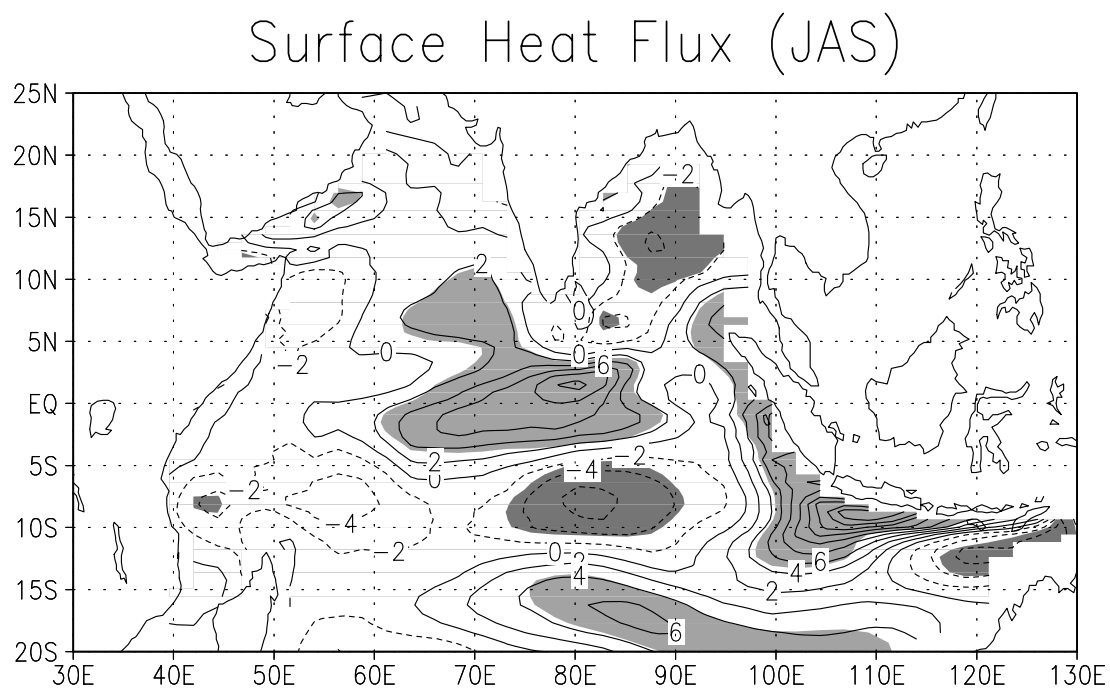




Fig. 14

(a)



(b)

